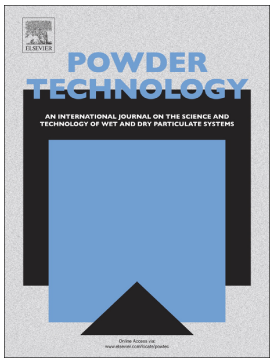

Investigation of granular dynamics in a continuous blender using the GPU-enhanced discrete element method

Chao Zheng, Liang Li, Bernardus Joseph Nitert, Nicolin Govender, Thomas Chamberlain, Ling Zhang, Chuan-Yu Wu

PII: S0032-5910(22)00849-X

DOI: https://doi.org/10.1016/j.powtec.2022.117968

Reference: PTEC 117968

To appear in: *Powder Technology*

Received date: 5 July 2022

Revised date: 12 September 2022

Accepted date: 26 September 2022

Please cite this article as: C. Zheng, L. Li, B.J. Nitert, et al., Investigation of granular dynamics in a continuous blender using the GPU-enhanced discrete element method, *Powder Technology* (2022), https://doi.org/10.1016/j.powtec.2022.117968

Investigation of granular dynamics in a continuous blender using the GPU-enhanced Discrete Element Method

Chao Zheng[a], Liang Li[b], Bernardus Joseph Nitert[b], Nicolin Govender[a], Thomas Chamberlain[a], Ling Zhang[a], Chuan-Yu Wu[a, *]

[a] Department of Chemical and Process Engineering, University of Surrey, Guildford GU2 7XH, United Kingdom

[b] Janssen Pharmaceutica NV, Turnhoutseweg 30, 2340 Beerse, Belgium

Abstract

Continuous powder blending is an essential operation during continuous pharmaceutical manufacturing. However, the complex granular dynamics in the blender is still poorly understood. This study employs a graphic processor unit (GPU) enhanced discrete element method (DEM) to analyse the granular dynamics in a continuous blender. Numerical results indicate that only a small fraction of powder distributes in the upper region of the blender, while most of that distributes in the middle and lower regions. Besides, a higher impeller speed leads to a smaller hold-up mass and a shorter mean residence time. Interestingly, the maximum number of blade passes is achieved at an intermediate impeller speed. There are two distinct regimes during continuous blending: i) a shearing regime at low impeller speeds; and ii) a dynamic regime at high impeller speeds. This study demonstrates that the GPU-enhanced DEM can be a robust tool for analysing powder flow during continuous pharmaceutical manufacturing.

Keywords: DEM, Continuous blending, Continuous manufacturing, Residence time distribution, Powder flow, GPU computing.

[*] Corresponding author: E-mail: c.y.wu@surrey.ac.uk (C.-Y. Wu)

1. Introduction

In the past decades considerable efforts were made in various industries to adopt continuous manufacturing (CM) with the aim to improve manufacturing efficiency and reduce the lead time. CM lines were successfully utilised in food, catalysis, and fertiliser production. Relatively recently, it became an attractive production technique for pharmaceutical manufacturing [1-4], as the CM process provides more extensive control of product quality with implementation of process analytical technology [5, 6]. Furthermore, it increases flexibility in batch size as no geometrical scale up/down is required, only changing the process runtime.

Continuous pharmaceutical manufacturing lines generally consist of various unit operations, including continuous blending that is widely used to process pharmaceutical powders to alleviate powder segregation and agglomeration during production [7, 8]. Continuous powder blending was extensively investigated experimentally to obtain a good understanding of powder flow in continuous blenders [9-11]. In particular, the effects of blender design, powder properties, and operation parameters on blending performance were explored. Portillo et al. [11] performed an experimental study on continuous powder mixing of Edible and Fast Flo Lactose with a GEA blender, which had a length of 0.74 m, a diameter of 0.15 m, and the impeller speed ranging from 16 rpm to 78 rpm. They found that the impeller speed and the blender angle significantly influence the residence time distribution (RTD) and the number of blade passes. Surprisingly, they also observed that the cohesion of powders considered did not significantly impact the blending performance. Portillo et al. [12] statistically investigated powder mixing with two different GEA blenders: one identical to that used in reference [11], and the other with a length of 0.31 m and a diameter of 0.05 m, and the impeller speed ranging from 16 rpm to 340 rpm. Their results showed that the residence time was significantly dependent on the impeller speed and the inclination angle,

but the powder cohesion had an insignificant impact on the blending performance. Osorio et al. [13] investigated the effect of process parameters and blade configuration on the blending characteristics of a Glatt GCG-70 blender and showed that a higher impeller speed resulted in a larger mean centred variance and a higher number of blade passes, but lower hold-up and shorter mean residence time in the blender. It is also found that a higher feed rate led to a larger hold-up, but a shorter mean residence time and a smaller number of blade passes. In addition, the blade configuration had a significant influence on the hold-up and the mean residence time. Pedersen et al. [14] used the near-infrared spectroscopy technology to investigate the residence time distribution of a continuous powder mixing process and illustrated that the mean residence time of powder could be used as a valuable parameter to characterise the CM process. Escotet-Espinoza et al. [15] experimentally investigated how the tracing material properties impacted the RTD response during the continuous powder blending. They showed that the tracing material properties significantly affect the obtained RTD results, which arose from different dynamic characteristics of tracing materials inside the continuous blender. Therefore, it is essential to select a proper tracing material to match the base material for characterising the continuous blending system.

Numerical approaches, such as discrete element modelling (DEM), population balance modelling and surrogate models, can provide more detailed information on the blending process [16-19], which can enable an enhanced understanding of the blending process, guide the selection of blender configurations and processing parameters. Among the above-mentioned numerical approaches, the DEM approach is advantageous in capturing granular dynamics, and is employed to analyze continuous blending processes. For instance, Toson et al. [20] investigated the mixing dynamics in a vertical in-line continuous powder mixer using DEM. In their study, a scaling factor was selected, while the shape of particle size distribution was kept. In such a way, all particles were ensured to be smaller than the smallest gap in the mixer geometry. Their results indicated that the RTD curves can be used to study the

downstream response of the continuous mixing device to upstream fluctuations in the inlet material stream. Sarkar et al. [21] adopted DEM to analyse the powder dynamics in a continuous blender, which has the same geometry investigated experimentally by Portillo et al. [11]. To save computation resources, they only modelled a section of the continuous mixer. Particles are modelled as monodisperse spheres with a diameter of 4 mm. They revealed that the impeller speed and the fill level in the blender significantly impact the particle flow and axial mixing, wherein a lower impeller speed with higher fill levels, as well as larger impeller speeds with smaller fill levels contributed to a better mixing effect. Sarkar et al. [22] examined the powder flow behaviour inside a commercial bladed mixer using DEM, in which the mixer was modelled using periodic slices. To form a polydisperse particulate system, particle diameters are chosen randomly between $0.8d_p$ and $1.2d_p$, where d_p is the mean particle diameter of 3 mm or 4 mm. They found that this approach could reproduce the flow behaviour well for the central section of the blender but could not describe the flow behaviour in the sections close to the inlet and outlet satisfactorily, indicating that the assumption of boundary conditions is less valid in these regions. Gao et al. [23, 24] adopted DEM to model a section of continuous blender with periodic boundary conditions. For simplicity, the simulation considers only non-segregating mixtures using identical particles (3 mm or 4 mm in diameter). They found that the blending performance could be significantly improved by maintaining the axial velocity constant while increasing the blade speed and adjusting the blade angle or weir height during the blender design. Additionally, they found that the shaft angle and blade speed are the two most important factors dominating the blending performance. Using the periodic slice DEM method, Bhalode et al. [25] adopted a multi-zonal compartment modeling strategy to study the powder flow in continuous blender, which had the same configuration as used by Gao et al. [23]. Compared to the DEM simulation of the entire blender, they found that the proposed multi-zonal hybrid model could significantly save computational resources.

Experimental and numerical results can be further extracted to develop data-based models for in-depth evaluation or prediction of the CM lines. Based on the collected data from continuous manufacturing, Silva et al. [26] presented a statistical process monitoring strategy to reveal process trends. Beke et al. [27] proposed a digital twin development for a continuous pharmaceutical powder blending process by adopting the RTD model and the artificial neural networks (ANN) method. They found that the RTD model is more suitable for industrial development due to reasonable development efforts.

The CM process has been increasingly adopted in industrial production [28]. Generally, the studies based on physical experiments have their limitations, such as complex implementation procedures and the requirement of bespoke components, resulting in significant increase of cost and time. The previous numerical studies generally adopted a reduced geometric model or used periodic boundaries, mainly due to computational limits, to simulate the powder flow in the blender, which is quite different from the actual production. Therefore, our understanding on continuous blending is still limited. In addition, geometric design and parameter optimisation for continuous blending are still in their infancy, which urgently requires further investigation. To the best of the authors' knowledge, few DEM studies performed on a full-size continuous powder blender, incorporating complex impeller configuration. Hence, the GPU-enhanced DEM approach is employed here to explore the powder dynamics in a full-size blender, with the population of particles up to millions and operation time up to hundreds of seconds. This paper aims to explore the effect of impeller speed on blending process performance factors, e.g., the mean residence time, RTD, hold-up mass, mean centered variance, and the number of blade passes, are comprehensively investigated, aiming to guide the blender design and selection of operation parameters in actual pharmaceutical CM processes.

2. Numerical model

2.1 Discrete element method

DEM is one of the most effective methods to model the bulk material by solving the motion equations for individual particles. The translational and rotational motion of particles are governed by the Newton's second law as-

$$m_i \frac{d\boldsymbol{V}_i}{dt} = \boldsymbol{F}_{C,i} + m_i \boldsymbol{g} \tag{1}$$

$$I_i \frac{d(\boldsymbol{\omega}_i)}{dt} = \boldsymbol{T}_i \tag{2}$$

where m_i is the particle mass, I_i is the moment of inertia, $\boldsymbol{V}_i$ is the translational speed, $\boldsymbol{g}$ is the gravitational acceleration, $\boldsymbol{\omega}_i$ is the angular speed, $\boldsymbol{F}_{C,i}$ is the total contact force, and $\boldsymbol{T}_i$ is the torque.

In this study, the Blaze-DEM, a GPU-enhanced DEM code developed by Govender et al. [29-31], is adopted to simulate the powder flow in the blender. The Kelvin-Voigt linear viscoelastic spring dashpot model is adopted to model the normal contact force as-

$$\boldsymbol{F}_n = \left(K_n \Delta V^{1/3}\right)\boldsymbol{n} - C_n \left(\boldsymbol{V}_R \cdot \boldsymbol{n}\right)\boldsymbol{n} \tag{3}$$

where $K_n = \frac{m_{eff}}{t_{contact}^2}\left(\ln(\epsilon)^2 + \pi^2\right)$ is the spring stiffness, $\boldsymbol{n}$ is the contact normal, $C_n = \frac{2\ln(\epsilon)\sqrt{K_n m_{eff}}}{\sqrt{\ln(\epsilon)^2 + \pi^2}}$ is the damping coefficient, $\boldsymbol{V}_R$ represents the relative contact velocity, ϵ is the coefficient of restitution, $m_{eff} = \left(\frac{1}{m_1} + \frac{1}{m_2}\right)^{-1}$ denotes the effective particle mass, and $t_{contact}$ is the contact time.

The Cundall-Strack tangential model is used to calculate the tangential contact force as-

$$\boldsymbol{F}_T = -K_T\left(\boldsymbol{V}_T dt\right) - C_T \boldsymbol{V}_T + \boldsymbol{F}_T' \tag{4}$$

where $\boldsymbol{F}_{\mathrm{T}}^{'}$ represents the projected tangential force, K_{T} represents the tangential spring stiffness, and $K_{\mathrm{T}} \geq K_n/2$, $C_{\mathrm{T}}=\frac{2\ln(\epsilon)\sqrt{K_{\mathrm{T}} m_{\mathrm{eff}}}}{\sqrt{\ln(\epsilon)^2+\pi^2}}$ represents the tangential damping coefficient, and $\boldsymbol{V}_{\mathrm{T}}$ represents the tangential relative velocity.

The torque exerted on the individual particle is expressed as-

$$\boldsymbol{\Gamma} = \boldsymbol{r} \times \boldsymbol{F}_{\mathrm{n}} \tag{5}$$

where r represents the vector between the contact point and the mass centre. At time k, the following expression is used to calculate the angular velocity as

$$\boldsymbol{\omega}_k = \boldsymbol{\omega}_{k\text{-}1} + \boldsymbol{\alpha}_k^{\mathrm{ang}} \Delta t \tag{6}$$

The acceleration of angular velocity $\boldsymbol{\alpha}^{\mathrm{ang}}$ is calculated as $\boldsymbol{\alpha}_k^{\mathrm{ang}} = \boldsymbol{I}_k^{-1}\boldsymbol{\Gamma}_k^{\mathrm{net}}$, where $\boldsymbol{\Gamma}_k^{\mathrm{net}}=\Sigma_{j=1}^{L}\boldsymbol{\Gamma}^{ij}$ represents the resultant contact torque on the particle i and $\boldsymbol{I}_k$ represents the inertia tensor. The particle orientation is expressed with a unit quaternion $\boldsymbol{q}\{w,x,y,z\} = \{1,0,0,0\}$, where w represents an angle [-1:1], and (x, y, z) represents the rotational axis. The following expression gives the relationship between the quaternion and the axis angle representa ion (θ, x_1, y_1, z_1) as-

$$\boldsymbol{q}=\{\cos(\theta/2), x_1\sin(\theta/2), y_1\sin(\theta/2), z_1\sin(\theta/2)\} \tag{7}$$

The quaternion has a relationship with the angular velocity vector $\boldsymbol{\omega}$ as-

$$\boldsymbol{q}=\left\{\cos(\|\boldsymbol{\omega}_k\|), \sin\left(\|\boldsymbol{\omega}_k\|\frac{\boldsymbol{\omega}_k}{\|\boldsymbol{\omega}_k\|}\right)\right\} \tag{8}$$

Then, the angular orientation of the particle at time *k* is written as-

$$\boldsymbol{q}_k = \boldsymbol{q}_{k\text{-}1} \times \Delta\boldsymbol{q} \tag{9}$$

2.2 Blender model setup

The continuous blender is an important unit of the GEA ConsiGma® system. Figure 1 shows the general geometric information of the full-size continuous powder blender. The inner diameter of the barrel is 118 mm, and that of the inlet and outlet tube is 100 mm. The length of the main working domain is about 920 mm. In the current configuration, the inclined angle of blender is 15°. According to the function of the blade elements, the impeller assembled inside the barrel can be mainly divided into three different sections, which is the so-called 'forwards-alternating-forwards blade configuration. There are two types of elements used for the blade configuration. One is called the transport element; the other is called the transport-mix element. Sections 1 and 3 are both transport sections, while Section 2 is a transport-mix section. When the blending process begins, the powder is released from the inlet with random orientations. The feed rate is kept constant as 40 kg/h, which corresponds to a line throughput in commercial manufacturing. Five shaft speeds range from 150 rpm to 350 rpm with an increment of 50 rpm are considered in this study.

2.3 Material properties

Microcrystalline cellulose (MCC), VIVAPUR® MCC Spheres 1000 (JRS Pharma GmbH & Co. KG, Rosenberg, Germany), is used in this study as the model material. Figure 2 presents the micro-image of MCC particles using a digital microscope (VHX-7000, Keyence Deutschland GmbH, Neu-Isenburg, Germany). The powder presents a high degree of brightness and excellent sphericity. The ring shear test indicted that the VIVAPUR® MCC Spheres 1000 is a free-flowing powder. Figure 3 shows the corresponding volume percentage and cumulative particle size distribution. It can be seen that the powder has a narrow size distribution. The mean diameter of the VIVAPUR® MCC Spheres 1000 is about 1,197 μm. The true density of the powder is 1,450 kg/m^3, which is measured with a helium pycnometer (AccuPyc II 1340, Micromeritics, USA).

2.4 DEM parameter calibration

For DEM simulations, many input parameters need to be determined. As described in Section 2.3, some of the parameters, such as density and particle size, can be measured experimentally, and some parameters (i.e., normal stiffness and coefficients of restitution), which may be less significant, can be obtained from literature [32, 33]. However, other DEM parameters need to be calibrated, aiming to make the simulation reproduce the real bulk response for the specific material. In this paper, the friction coefficient between particle and particle (μ_{pp}), the friction coefficient between particle and wall (μ_{pw}), and the rolling resistance (μ_r) are calibrated.

To calibrate the DEM parameters μ_{pp}, μ_{pw} and μ_r, the numerical and experimental powder discharge are performed. Figure 4 illustrates the numerical and experimental setup for the powder discharge tests, which uses the Flodex-M tester (Hanson Research, Chatsworth, CA, USA). Each experiment uses 100 g sample. In this study, the orifice size is selected as 12 mm, which makes the simulation time scale not too long nor too short. According to the standard operation procedure of the tester, the powder is put in the stainless cylinder first and settles down, then the gate panel of the orifice is triggered to allow the powder flow through the orifice. The accumulative mass collected in the bottom box is automatically measured and recorded with a digital scale. The precision and sample frequency of the digital scale is 0.001 g and 2 Hz, respectively. The mass flow rate and the final accumulative powder mass in the bottom box are used as two main indices to calibrate the selected DEM parameters. Table 1 lists all the cases run for calibration purpose. The three DEM parameters are varied to get different bulk responses. Until a good match between the measured and simulated responses is achieved, the set of DEM parameters is chosen for later DEM simulations of the continuous blender.

Figure 5 plots the evolution of the discharged powder mass for three repeated experiments and one selected DEM case. It can be seen that the DEM simulation can reproduce the discharge process very well. With appropriately selected DEM parameters, a good agreement of the discharge mass curve can be achieved between the numerical and experimental data. Two parameters (the error of mass flow rate and the error of discharge mass) are calculated to select proper DEM parameters for the powder. The error between numerical and experimental data is defined as

$$e = \left| \frac{D_1 - D_2}{D_2} \right| \times 100\% \tag{10}$$

where e is the error, D_1 is the data obtained from DEM simulation, D_2 is the experimental data.

Once the error of mass flow rate and the error of discharge mass are obtained, an overall error is proposed to assist the DEM parameters selection better. The overall error is defined as the average value of these two above errors. Figure 6 shows the overall errors for all simulation cases. It can be noted that cases 1-5 give similar overall errors, which suggests that particle-wall friction coefficient is insignificant in the present study. Among all cases considered, it can be found that Case No. 3 presents the minimal overall error, which indicates that the corresponding DEM parameters are sufficient for further simulations. These values are chosen to final DEM input parameters for blender simulations and are listed in Table 2. Polydisperse particle systems with three different particle sizes extracted from PSD information are modelled in this study. For all cases, a total of about 6.0 kg powder, which consists of about 5,000,000 particles, is used in the blender simulations. The total simulation time is set as 600 s, with a particle time step of 5×10^{-6} s.

2.5 Data acquisition and processing

The residence time distribution is vital for understanding the blending process. During the simulation, a domain is defined for calculating particle residence time. When the particle enters and leaves the domain, the time the particle resides in the blender is recorded. The residence time distribution $E(t)$ of the particle in the continuous blender can then be expressed as [34, 35]

$$E(t)=\frac{\mathrm{N}(t)}{\int_0^{\infty} N(t)\,dt} \cong \frac{N_i}{\sum_{i=0}^{\infty} N_i \Delta t_i} \tag{11}$$

where $N(t)$ is the number of particles crossing the outlet at time t, N_i is the particle number in the residence time bin i, Δt is the residence time bin size.

The mean residence time τ, and the mean centred variance σ_τ^2 can be obtained using the following equations

$$\tau = \int_0^{\infty} t\,E(t)dt \tag{12}$$

$$\sigma_\tau^{\,2} = \frac{\int_0^{\infty} (t-\tau)^2 E(t)dt}{\tau^2} \tag{13}$$

The number of blade passes N_p can be defined to evaluate the amount of material passed by the blade during blending. It is a function of the shaft rotation speed ω and the mean residence time τ, which can be expressed as [16, 18]

$$N_p = \omega \times \tau \tag{14}$$

3. Results and discussion

In this section, comprehensive analyses were performed on the obtained DEM results, which included the particle flow pattern, particle dynamics and residence time

distribution. The effects of impeller speed were studied using critical performance indicators namely the mean residence time (τ), the RTD, the number of blade passes (N_p) and the mean centered variance (σ_τ^2).

3.1 Particle flow and hold-up mass

DEM simulations make it possible to observe what happens inside the continuous blender. It is valuable to visualise the particle flow in the continuous blender. Figure 7 shows the particle distribution profiles at different times during the simulation of blending process over 600 s. The simulation begins with an empty blender. With the powder feeding to the blender via the inlet, the amount of powder inside the blender increases and the powder particles occupy more space of the blender (see Fig. 7a). At the same time, some particles begin to escape from the outlet until a steady state is reached (see Figs. 7b and 7c).

The hold-up mass is one of the most critical indices to identify and monitor whether the blending system has achieved a steady-state. Figure 8 plots the hold-up mass distributed in three sections of the blender during the entire blending process. It shows that the hold-up mass linearly increases to 2.1 kg due to the fixed feed rate at the beginning phase of the process up to approximately t=300 s. Then the hold-up mass value keeps almost unchanged until t=550 s, indicating the blending system reaches the steady state during this period. After t=550 s, powder feeding is stopped, hold-up mass starts to decrease. The evolution of hold-up mass further explains the change of powder distribution in the blender, as illustrated in Fig. 7.

Figure 9 depicts the hold-up mass distribution ratios at steady-state with various impeller speeds. The hold-up mass distribution ratio is defined as the powder mass distributed in a specified section divided by the hold-up mass in the blender. Interestingly, it is found that most of the powder distributes in the middle and bottom section. Only a small fraction (<5%) of powder distributes in the top section. It can be explained that the powder in the inclined blender tends to accumulate and settles at a lower height of the blender due to gravity. This

finding implies that the mixing mainly occurs in the bottom and middle sections. According to the function of these sections, the middle section is designed to facilitate powder mixing. Compared to the mass ratios of the middle section at other impeller speeds, the mass ratio at 250 rpm is the largest (about 50%). Additionally, it is worth considering in future work how screw elements in various blender configurations affect blending performance.

The evolution of hold-up mass in the blender at various impeller speeds is illustrated in Figure 10. All the curves show a similar trend: the hold-up material first linearly increases with time, then reaches a nearly constant value for a while, finally decreases with the time. At the first 50 s, all curves collapse into one line with a slope equal to the fixed feed rate. It is because the powder paticles accumulate in the inclined blender at the beginning of blending process. For the higher impeller speed, it is quicker to reach the steady state. At steady-state, a higher impeller speed leads to a smaller hold-up mass in the blender. It is found that the curves for 200 rpm and 250 rpm are very close to each other, implying a similar flow pattern during continuous blending in this speed range.

Figure 11 plots the hold-up mass and the time spent to achieve steady-state as a function of the impeller speed. The time to steady-state is the time period from the beginning of the process to its steady-state. Both the hold-up mass and the time to steady-state have a similar trend, which dramatically decrease with increasing the impeller speed. Surprisingly, 250 rpm is the transaction point for both hold-up mass and time to steady-state, where a bigger drop in the hold-up and time to steady-state can be observed, implying that there are two different regimes during the continous blending. The regime transition of powder flow within the blender exists at an intermediate impeller speed, as also observed by Dubey et al. [19]. Even so, a higher impeller speed generally leads to a smaller hold-up mass in the blender, which is consistent with the observation of Osorio et al. [13].

3.2 Particle velocity and trajectory

At steady-state, the average particle speed and its relative standard deviation (RSD) usually keep stable. Figure 12 plots the average particle speed and its RSD at steady-state with an impeller speed of 250 rpm. The particles in the middle section of the blender present the largest average speed; those of the top and bottom section have a lower speed. This result is consistent with the blender configuration. The middle section of the impeller consists of transport-mix elements, which promote shearing and conveying. At the same time, the blade configuration in the middile section would lead to a higher resultant particle speed in the circumferential direction. Additonally, particles in the middle and bottom sections present smaller RSD of speed. It may be explained that a denser environment would form in the middle and bottom section due to gravitional force. In a denser environment, a particle would have more constant collions with neighboured particles and wall. Therefore, a smaller RSD can be observed.

During the continuous blending process, particles are expected to travel through the blender from the inlet to the outlet. It is interesting to observe how the individual particles move inside the continuous blender. Figure 13 plots two types of particle trajectories for selected particles. Fig. 13a gives a typical particle trajectory where the particle crosses the entire blender. The particle path shows a spiral motion along the axis of the impeller, due to axial transport. Meanwhile, the particle rotates in the circumferential direction due to blade rotation. Also, it is notable that particle trajectory is very dense at the bottom and middle sections, while it becomes sparse in the top section. This can be explained that most of the particles distribute in the bottom and middle sections, resulting in a low axial speed in the blender. Dense particle packing contributes to more frequent particle collisions, which constrain the particle motion and form a small particle displacement in the axial direction. By contrast, some particles may have difficulities in travelling through the blender and follow the trajectory in Fig. 13b. These particles can be trapped in the blender arising from complex particle-particle and particle-wall interactions, and may cause non-desired blending

performance.

As proposed by Einstein [36], the path length is the total distance covered when a particle moves from the initial position to the final position. When the particle travels in the blender, the particle path is crucial for analyzing the process. The particle velocity and position are recorded during the simulation. The motion history of a particle is saved with a time interval Δt= 0.01 s. Therefore, the position of a particle at time t is written as (x, y, z). At time $t+\Delta t$, the increment of particle position in XYZ coordinates can be recorded as (Δx, Δy, Δz). Then, the distance (L_i) for the particle i during the time interval (Δt) can be calculated as follows:

$$L_i = \sqrt{(\Delta x_i \times \Delta x_i) + (\Delta y_i \times \Delta y_i) + (\Delta z_i \times \Delta z_i)} \tag{15}$$

The entire period can be discretised into N time intervals. Consequently, the total length of particle path in the blender can be obtained by summing the distance of particle at each time interval as:

$$L = \sum_{i=1}^{N} L_i \tag{16}$$

It is clear that L depends upon the time interval used to collect the data. Based upon their experimental measurement in a similar set-up, Portillo et al. [10] showed that a time interval of 0.0169 s is small enough to capture the particle path with a sufficient resolution. Therefore, the time interval of 0.01 s used in this study is adequate for calculating the particle path.

Figure 14 plots particle path length as a function of residence time in the blender. Six particle paths are selected from each case with different impeller speeds. It is clear that a longer residence time leads to a longer particle path in the blender. A close examination of the data shows that the linear fitting can be used to describe the relationship between the particle path and residence time confirmed by a goodness of fit R^2=0.95. This is also consistent with the report of Portillo et al. [10], who used the Positron Emission Particle Tracking (PEPT) technique to track the particle path in a GEA blender.

3.3 Residence time distribution

The RTD is a vital parameter for any continuous process. Figure 15 shows the effect of impeller speed on the residence time distribution (E-curve) in the continuous blender with a feed rate of 40 kg/h. It is clear that the impeller speed has a significant impact on the RTD. A higher impeller speed leads to a shorter residence time of particles in the bender. Interestingly, the RTD at a lower impeller speed (i.e., 150 rpm) is a bit different from those at higher impeller speeds (i.e., 300 rpm and 350 rpm). It could be attributed to the different regime that exists at low and high impeller speeds, resulting in different RTD regimes as well [19]. The presented residence time distribution under various impeller speeds agrees with the results reported in previous literature [19].

As described in Equation (12), the mean residence time can be obtained by integrating the first moment of the RTD function. Figure 16 plots the corresponding mean residence time under various impeller speeds. The mean residence time decreases from about 240 s to 70 s, with the impeller speed increasing from 150 rpm to 350 rpm. Typically, higher impeller speeds resulted in shorter residence times and shorter total path lengths. These findings are in agreement with previous experimental studies [9-11]. The abrupt decrease in the mean residence time can be attributed to the substantial drop of hold-up mass in the continuous blender. Interestingly, the decreasing rate before 250 rpm is -0.46 s/rpm and that after 250 rpm is -1.08 s/rpm, which is in line with the two regimes. This is consistent with the change of hold-up mass, as shown in Figure 11.

The mean centered variance is a combined effect of convection and random movement of particles [19], and can be considered a quantitative measure of particulate dispersion [37]. According to Equation (13), the mean centred variance of the residence time distribution is plotted in Fig. 17. The mean centred variance increased with the impeller speed increasing from 150 rpm to 350 rpm. Meanwhile, high impeller speed would result in short residence

time, which is not beneficial for good mixing. Hence, 350 rpm may not be the best impeller speed, even though it contributes to the highest dispersion or axial mixing. Furthermore, the mean centred variance is also affected by the feed rate and powder properties [19, 37, 38]. Hence, the process parameters need to be studied in conjunction in future work.

When the powder is fed into the blender, it is subjected to the blade shearing and conveying. The amount of shear experienced by the powder particles is crucial for blender and process design. Figure 18 illustrates the average number of blade passes experienced by the particles when passing through the continuous blender. Based on Equation (14), the number of blade passes is strongly affected by the impeller speed and the residence time. The number of blade passes increases when the impeller speed increases from 150 rpm to 250 rpm, then decreases when the impeller speed further increases from 250 rpm to 350 rpm. The particles experience the maximum amount of shear (mechanical work) in the continuous blender at the intermediate impeller speed of 250 rpm. Consequently, a larger number of blade passes would contribute to a higher degree of powder homogeneity at the blender's exit [10, 11, 38]. This finding can be used to select the optimal impeller speed for continuous blending. A similar phenomenon has been observed and experimentally confirmed in previous literature [9]. It is evident that there are two distinct regimes in the continuous blending: i) a shearing regime when the impeller speed is lower than 250 rpm, and ii) a dynamic regime when the impeller speed is higher than 250 rpm. This observation corresponds well with the findings of hold-up mass (see Fig. 11) and the mean residence time (see Fig. 16). Under lower impeller speeds (<250 rpm), the powder is relatively less mixed in the continuous blender, and powder shearing dominates the process. The total shear experienced by the particle would increase with the increase in impeller speed. At higher impeller speeds (>250 rpm), the powder bed in the blender moves in a dynamic manner. At the intermediate speed 250 rpm, the powder bed gets sufficient mixing; exceeding the intermediate speed, the mixing performance may even be reduced. A higher impeller speed causes fewer internal contacts

between particles and a shorter residence time [39], consequently decreasing the number of blade passes.

4. Conclusions

The granular dynamics in a full-size continuous blender for pharmaceutical drug product manufacturing were analysed in detail. It is found that, at the steady-state, only a small fraction of powder distributes in the upper region of the blender, while most of the powder distributes in the middle and lower regions. Moreover, a larger impeller speed contributes to a smaller hold-up mass in the blender and a shorter residence time. Interestingly, the maximum number of blade passes is achieved at an intermediate impeller speed (i.e., 250 rpm used in this study), suggesting a possible optimal impeller speed for desired mixing. Through the detailed DEM analyses, it is revealed that there are two distinct regimes in continuous blending: i) a shear regime when the impeller speed is relatively low; and ii) a dynamic regime when the impeller speed is high. It is shown that the hold-up mass, the time to reach the steady state, or the mean residence time decreases at a higher rate in the dynamic regime than that in the shear regime. It is also interesting to find that, in the shear regime, the number of blade passes increases with the impeller speed, while in the dynamic regime it decreases as the impeller speed increases.

This study demonstrates that the simulation of full-size continuous systems is feasible and can provide further insights into powder flow in actual continuous blending, which can guide the geometric design and selection of process parameters. Further investigation can be focused on the powder properties and blender configuration on the mixing behaviour of pharmaceutical formulations. In addition, whether the demarcation impeller speed depends on the blender design and powder properties is worthy further investigation.

Acknowledgements

The authors want to acknowledge the financial support from the Flanders Innovation & Entrepreneurship and Janssen Pharmaceutica NV in Belgium (Grant No. HBC.2019.2927). University of Surrey would also like to acknowledge that Chao Zheng received a Marie Skłodowska-Curie Individual Fellowship under European Union's Horizon 2020 research and innovation programme (Grant No. 840264). We are also thankful for the valuable scientific inputs provided by Koen Heymans, Ko Cattoor, Yvonne Rosiaux, Bernd Van Snick and Elisabeth Schäfer from Janssen R&D.

References

[1] Kleinebudde, P., Khinast, J., Rantanen, J., 2017. Continuous manufacturing of pharmaceuticals. John Wiley & Sons.

[2] Schaber, D.S., Gerogiorgis, D.I., Ramachandran, R., Evans, J.M.B., Barton, P.I., Trout, B.L., 2011. Economic analysis of integrated continuous and batch pharmaceutical manufacturing: a case study. Industrial & Engineering Chemistry Research, 50(17), 10083-10092.

[3] Burcham, C.L., Florence, A.J., Johnson, M.D., 2018. Continuous manufacturing in pharmaceutical process development and manufacturing. Annual Review of Chemical and Biomolecular Engineering, 9, 253-281.

[4] Pernenkil, L., Cooney, C.L., 2006. A review on the continuous blending of powders. Chemical Engineering Science, 61(2), 720-742.

[5] Vargas, J.M., Nielsen, S., Cárdenas, V., Gonzalez, A., Aymat, E.Y., Almodovar, E., Classe, G., Colón, Y., Sanchez, E., Romañach, R.J., 2018. Process analytical technology in continuous manufacturing of a commercial pharmaceutical product. International Journal of Pharmaceutics, 538(1-2), 167-178.

[6] Pauli, V., Roggo, Y., Pellegatti, L., Trung, N.Q.N., Elbaz, F., Ensslin, S., Kleinebudde, P., Krumme, M., 2019. Process analytical technology for continuous manufacturing

tableting processing: A case study. Journal of Pharmaceutical and Biomedical Analysis, 162, 101-111.

[7] Sarkar, A., Wassgren, C., 2010. Continuous blending of cohesive granular material. Chemical Engineering Science, 65(21), 5687-5698.

[8] Liu, J., Su, Q., Moreno, M., Laird, C., Nagy, Z., Reklaitis, G., 2018. Robust state estimation of feeding–blending systems in continuous pharmaceutical manufacturing. Chemical Engineering Research and Design, 134, 140-153.

[9] Vanarase, A.U., Muzzio, F.J., 2011. Effect of operating conditions and design parameters in a continuous powder mixer. Powder Technology, 208, 26-36.

[10] Portillo, P.M., Vanarase, A.U., Ingram, A., Seville, J.K., Ierapetritou, M.G. Muzzio, F.J., 2010. Investigation of the effect of impeller rotation rate, powder flow rate, and cohesion on powder flow behavior in a continuous blender using PEPT. Chemical Engineering Science, 65(21), 5658-5668.

[11] Portillo, P.M., Ierapetritou, M.G., Muzzio, F.J., 2007. Characterization of continuous convective powder mixing processes. Powder Technology, 182(3), 368-378.

[12] Portillo, P.M., Ierapetritou, M.G., Muzzio, F.J., 2009. Effects of rotation rate, mixing angle, and cohesion in two continuous powder mixers-A statistical approach. Powder Technology, 194(3), 217-227.

[13] Osorio, J.G., Muzzio, F.J., 2016. Effects of processing parameters and blade patterns on continuous pharmaceutical powder mixing. Chemical Engineering and Processing-Process Intensification, 109, 59-67.

[14] Pedersen, T., Karttunen, A.P., Korhonen, O., Wu, J.X., Naelapää, K., Skibsted, E., Rantanen, J., 2021. Determination of residence time distribution in a continuous powder mixing process with supervised and unsupervised modeling of in-line near infrared (NIR) spectroscopic data. Journal of Pharmaceutical Sciences, 110(3), 1259-1269.

[15] Escotet-Espinoza, M.S., Moghtadernejad, S., Oka, S., Wang, Y., Roman-Ospino, A., Schäfer, E., Cappuyns, P., Van Assche, I., Futran, M., Ierapetritou, M., Muzzio, F., 2019. Effect of tracer material properties on the residence time distribution (RTD) of continuous powder blending operations. Part I of II: Experimental evaluation. Powder Technology, 342, 744-763.

[16] Bhalode, P., Ierapetritou, M., 2021. Hybrid multi-zonal compartment modeling for continuous powder blending processes. International Journal of Pharmaceutics, 602, 120643.

[17] Dubey, A., Sarkar, A., Ierapetritou, M., Wassgren, C.R., Muzzio, F.J., 2011. Computational approaches for studying the granular dynamics of continuous blending processes, 1–DEM based methods. Macromolecular Materials and Engineering, 296(3-4), 290-307.

[18] Sen, M., Ramachandran, R., 2013. A multi-dimensional population balance model approach to continuous powder mixing processes. Advanced Powder Technology, 24(1), 51-59.

[19] Dubey, A., Vanarase, A.U., Muzzio, F.J., 2012. Impact of process parameters on critical performance attributes of a continuous blender—A DEM-based study. AIChE Journal, 58(12), 3676-3684.

[20] Toson, P., Siegmann, E., Trogrlic, M., Kureck, H., Khinast, J., Jajcevic, D., Doshi, P., Blackwood, D., Bonnassieux, A., Daugherity, P.D., Am Ende, M.T., 2018. Detailed modeling and process design of an advanced continuous powder mixer. International Journal of Pharmaceutics, 552(1-2), 288-300.

[21] Sarkar, A., Wassgren, C.R., 2009. Simulation of a continuous granular mixer: Effect of operating conditions on flow and mixing. Chemical Engineering Science, 64(11), 2672-2682.

[22] Sarkar, A., Wassgren, C.R., 2012. Comparison of flow microdynamics for a continuous granular mixer with predictions from periodic slice DEM simulations. Powder Technology, 221, 325-336.

[23] Gao, Y., Muzzio, F.J., Ierapetritou, M.G., 2012. Optimizing continuous powder mixing processes using periodic section modeling. Chemical Engineering Science, 80, 70-80.

[24] Gao, Y., Boukouvala, F., Engisch, W., Meng, W., Muzzio, F.J., Ierapetritou, M.G., 2013. Improving continuous powder blending performance using projection to latent structures regression. Journal of Pharmaceutical Innovation, 8(2), 99-110.

[25] Bhalode, P., Ierapetritou, M., 2021. Multi-zonal compartmentalization methodology for surrogate modelling in continuous pharmaceutical manufacturing. Computer Aided Chemical Engineering, 50, 725-731.

[26] Silva, A.F., Vercruysse, J., Vervaet, C., Remon, J.P., Lopes, J.A., De Beer, T., Sarraguça, M.C., 2019. In-depth evaluation of data collected during a continuous pharmaceutical manufacturing process: a multivariate statistical process monitoring approach. Journal of Pharmaceutical Sciences, 108(1), 439-450.

[27] Beke, Á.K., Gyürkés, M., Nagy, Z.K., Marosi, G., Farkas, A., 2021. Digital twin of low dosage continuous powder blending-artificial neural networks and residence time distribution models. European Journal of Pharmaceutics and Biopharmaceutics, 169, 64-77.

[28] Bhalode, P., Ierapetritou, M., 2020. A review of existing mixing indices in solid-based continuous blending operations. Powder Technology, 373, 195-209.

[29] Govender, N., Wilke, D., Kok, S., 2016. Blaze-demgpu: Modular high performance DEM framework for the GPU architecture. SoftwareX, 5, 62–66.

[30] Govender, N., Rajamani, R.K., Wilke, D.N., Wu, C.Y., Khinast, J., Glasser, B.J., 2018. Effect of particle shape in grinding mills using a GPU based DEM code. Minerals Engineering, 129, 71–84.

[31] Zheng C., Yost, E., Muliadi, A.R., Govender, N., Zhang, L., Wu, C.Y., 2022. Numerical analysis of die filling with a forced feeder using GPU-enhanced discrete element methods. International Journal of Pharmaceutics, 622, 121861.

[32] Hildebrandt, C., Gopireddy, S.R., Scherließ, R., Urbanetz, N.A., 2019. Investigation of powder flow within a pharmaceutical tablet press force feeder–A DEM approach. Powder Technology, 345, 616-632.

[33] Mukherjee, R., Sansare, S., Nagarajan, V., Chaudhuri, B., 2021. Discrete Element Modeling (DEM) based investigation of tribocharging in the pharmaceutical powders during hopper discharge, International Journal of Pharmaceutics, 596, 120284.

[34] Zheng, C., Zhang, L., Govender, N., Wu, C.Y., 2021. Dem analysis of residence time distribution during twin screw granulation. Powder Technology, 377, 924-938.

[35] Zheng, C., Govender, N., Zhang, L., Wu, C.Y., 2022. GPU-enhanced DEM analysis of flow behaviour of irregularly shaped particles in a full-scale twin screw granulator. Particuology, 61, 30-40.

[36] Einstein, H.A., 1937. Bedload transport as a probability problem. Sedimentation, 1027, 1-105.

[37] Puaux, J.P., Bozga, G., Ainser, A., 2000. Residence time distribution in a corotating twin-screw extruder. Chemical Engineering Science, 55, 1641–1651.

[38] Vanarase, A.U., Muzzio, F.J., 2011. Effect of operating conditions and design parameters in a continuous powder mixer. Powder Technology, 208, 26–36.

[39] Vanarase, A.U., Osorio, J.G., Muzzio, F.J., 2013. Effects of powder flow properties and shear environment on the performance of continuous mixing of pharmaceutical powders. Powder Technology, 246, 63–72.

Figure captions:

Table captions：

Table 1 Detailed parameters and bulk response for cases considered.

Table 2 List of the DEM input parameters.

CRediT authorship contribution statement

Chao Zheng: Conceptualization, Methodology, Draft preparation. Liang li: Investigation, Manuscript review and editing. Bernardus Joseph Nitert: Investigation. Nicolin Govender: Software. Thomas Chamberlain: Experiment. Ling Zhang: Data analyses. Chuan-Yu Wu: Supervision, Manuscript review and editing.

Declaration of interests

☒ The authors declare that they have no known competing financial interests or personal relationships that could have appeared to influence the work reported in this paper.

☒The authors declare the following financial interests/personal relationships which may be considered as potential competing interests:

Dr. Chao Zheng on Behalf of the Authors, 5th July 2022.

Table 1 Detailed parameters and bulk response for cases considered.

Case No.	μ_{pp} (-)	μ_{pw} (-)	μ_r (-)	Mass flow rate (g/s)	Discharge mass (g)
1	0.20	0.20	0.015	13.58	85.57
2	0.20	0.25	0.015	13.56	84.98
3	0.20	0.30	0.015	13.41	84.41
4	0.20	0.35	0.015	13.35	84.12
5	0.20	0.40	0.015	13.34	83.74
6	0.25	0.30	0.015	12.86	83.56
7	0.30	0.30	0.005	12.97	87.39
8	0.30	0.30	0.010	12.78	85.73
9	0.30	0.30	0.015	12.43	82.65
10	0.30	0.30	0.020	12.28	82.05
11	0.30	0.30	0.025	12.24	81.58
12	0.35	0.30	0.015	12.04	82.09
13	0.40	0.30	0.015	11.71	81.53

Table 2 List of the DEM input parameters.

Category	DEM parameters	Value	Unit
Measured	Particle density	1,450	kg/m^3
	Mean particle diameter	1197	μm
Obtained literately	Normal stiffness between particle and particle	1000	N/m
	Normal stiffness between particle and wall	1000	N/m
	Coefficient of restitution between particle and particle	0.3	-
	Coefficient of restitution between particle and wall	0.3	-
Common	Gravity acceleration	9.81	m/s^2
Obtained Iteratively	Sliding friction between particle and particle	0.20	-
	Sliding friction between particle and wall	0.30	-
	Rolling resistance	0.015	-

Graphical abstract

Highlights

- GPU-enhanced DEM analysis on the full scale continuous blending is performed.
- Impeller speed has a significant impact on the powder flow in the inclined blender.
- At steady-state, powder mainly distributes in the middle and bottom zones of blender.
- Maximum number of blade passes can be achieved at an intermediate impeller speed.

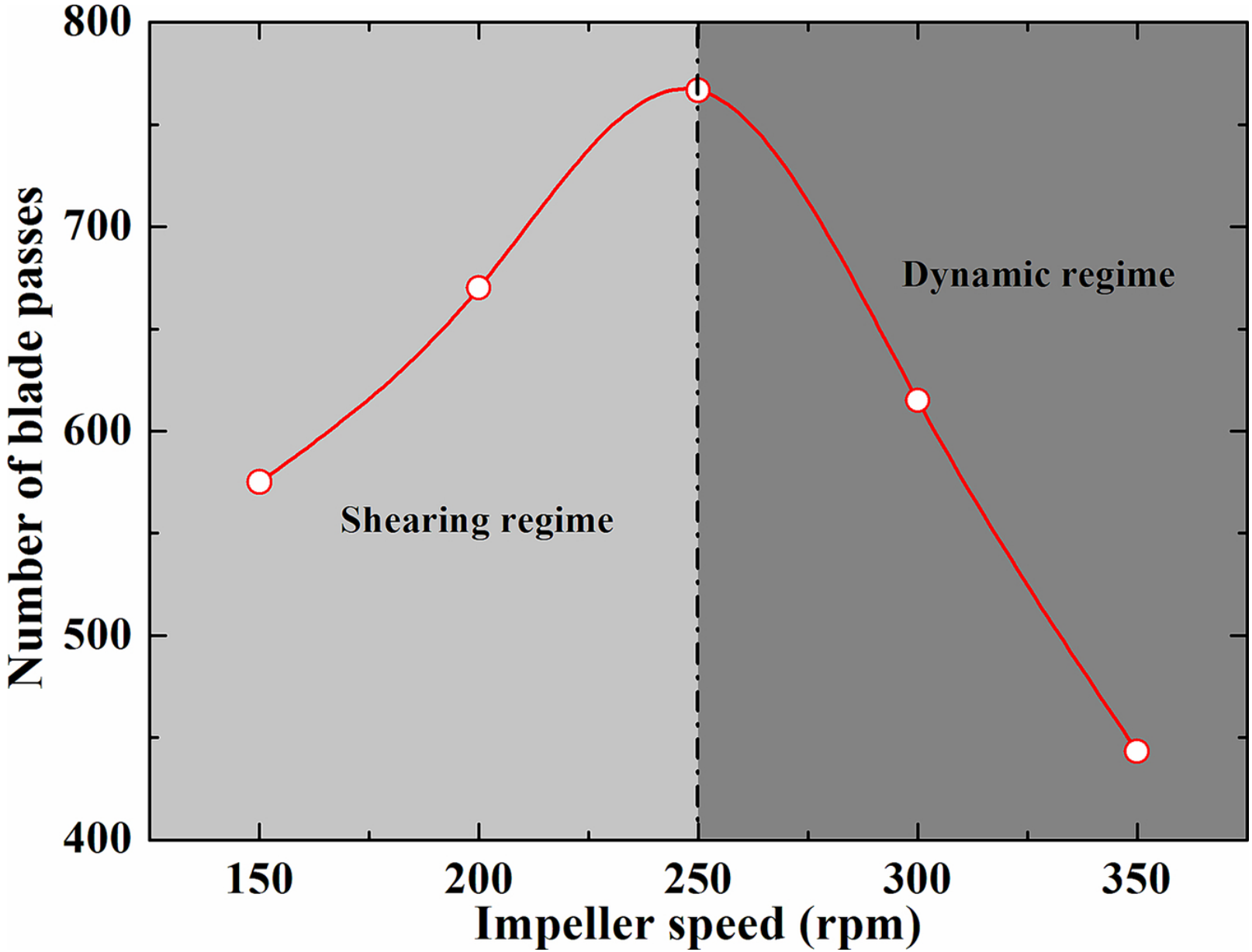

Graphics Abstract

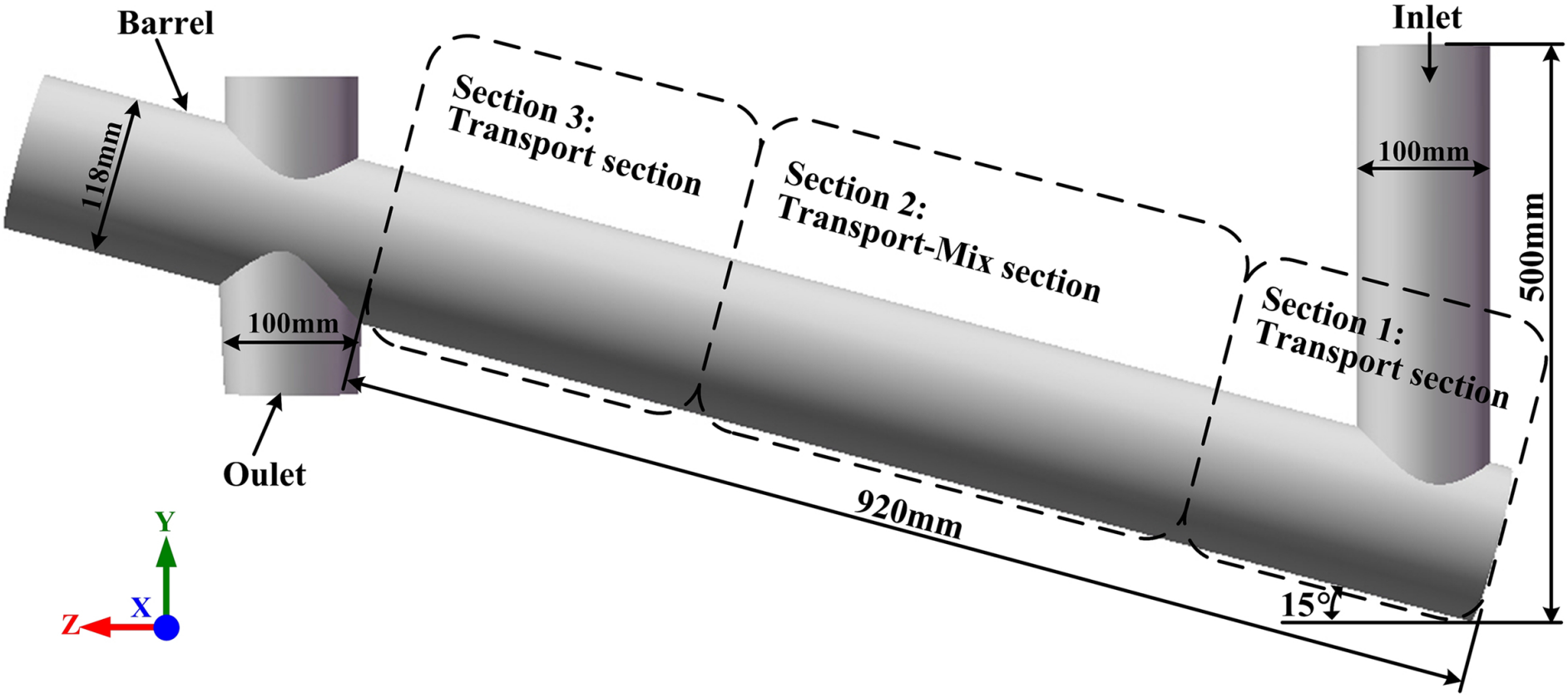
Barrel
Inlet
118mm
100mm
Section 3:
Transport section
Section 2:
Transport-Mix section
Section 1:
Transport section
100mm
500mm
Oulet
920mm
15°
Y
X
Z

Figure 1

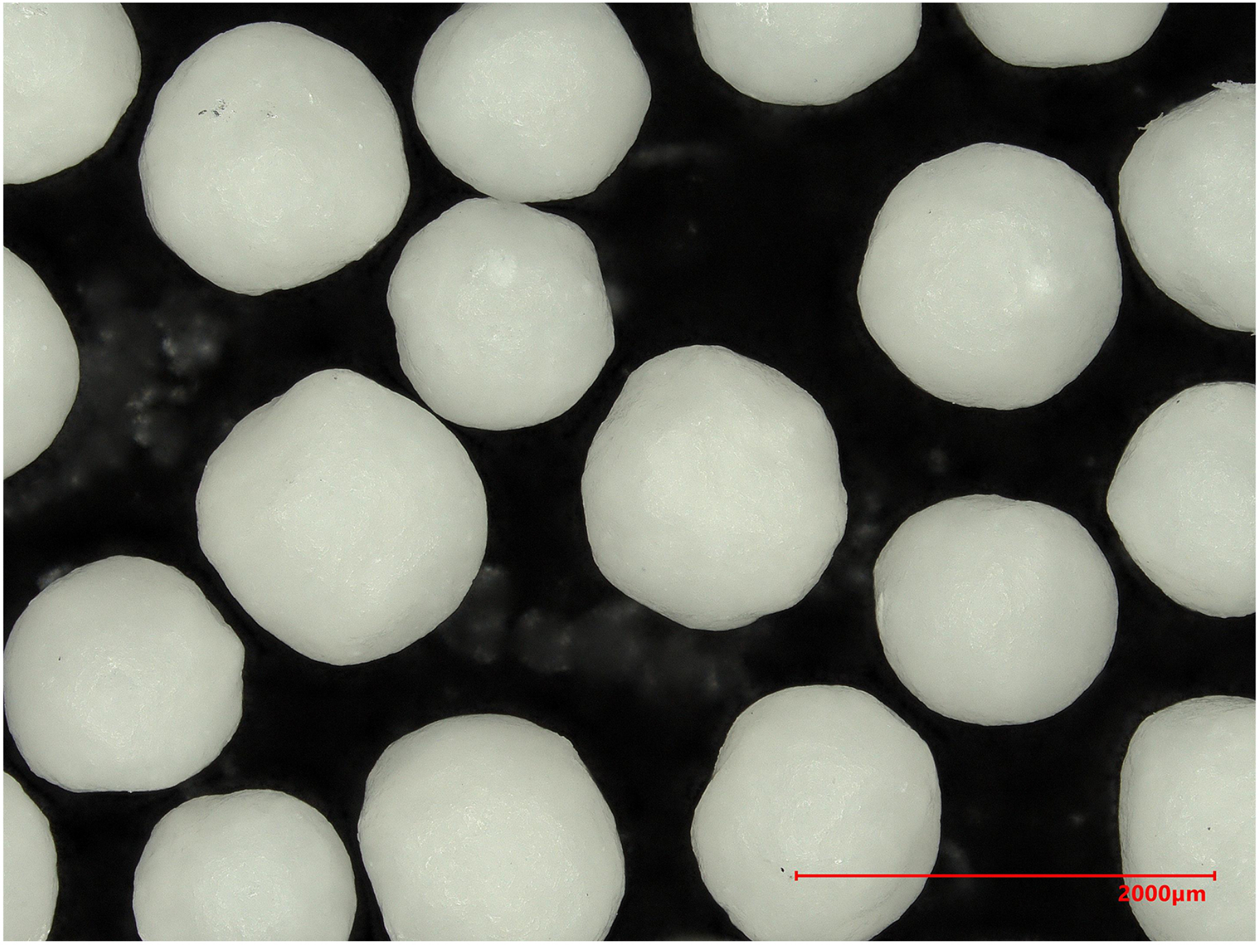

Figure 2

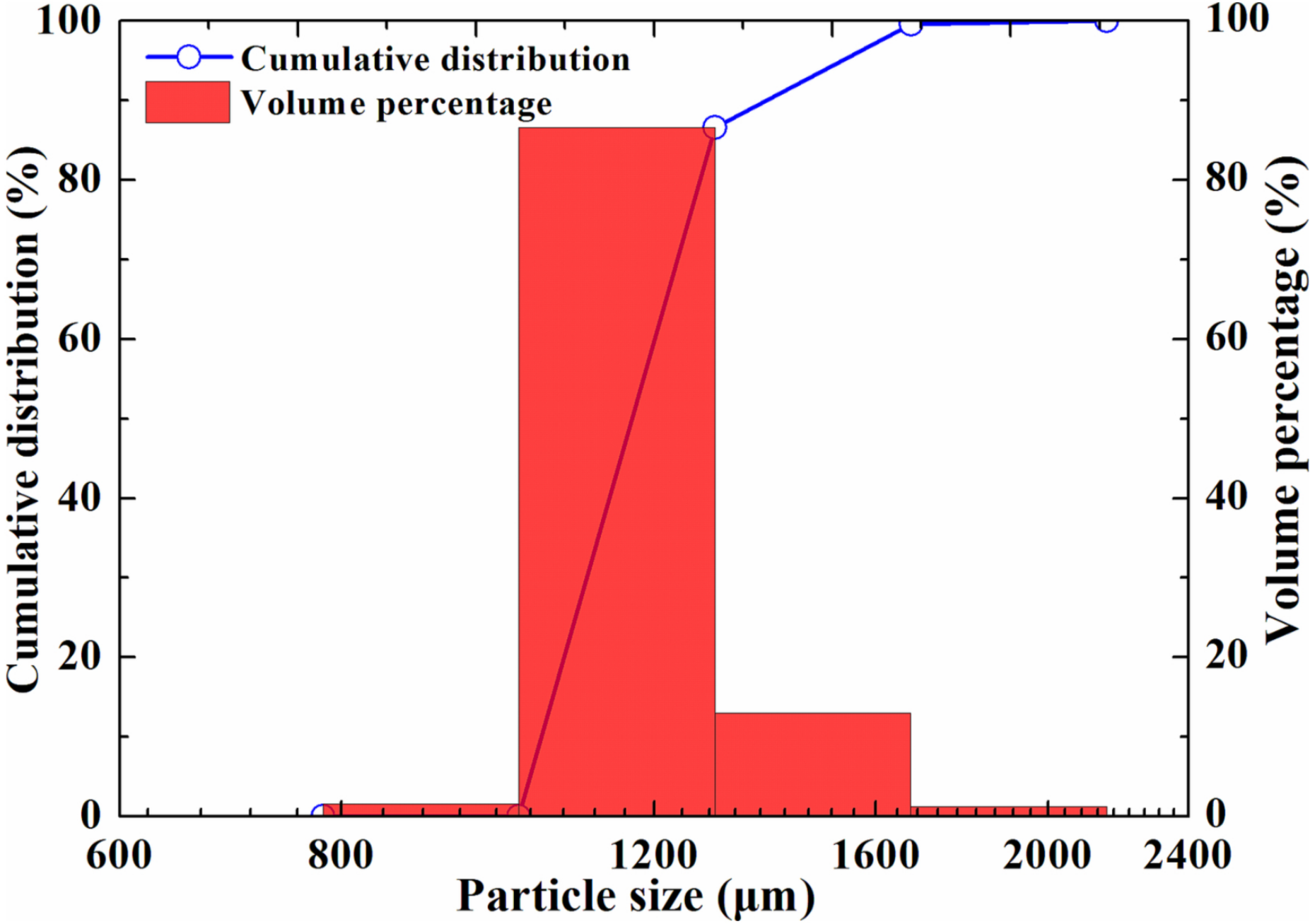
Cumulative distribution
Volume percentage
Cumulative distribution (%)
Volume percentage (%)
Particle size (μm)
0
20
40
60
80
100
600
800
1200
1600
2000
2400

Figure 3

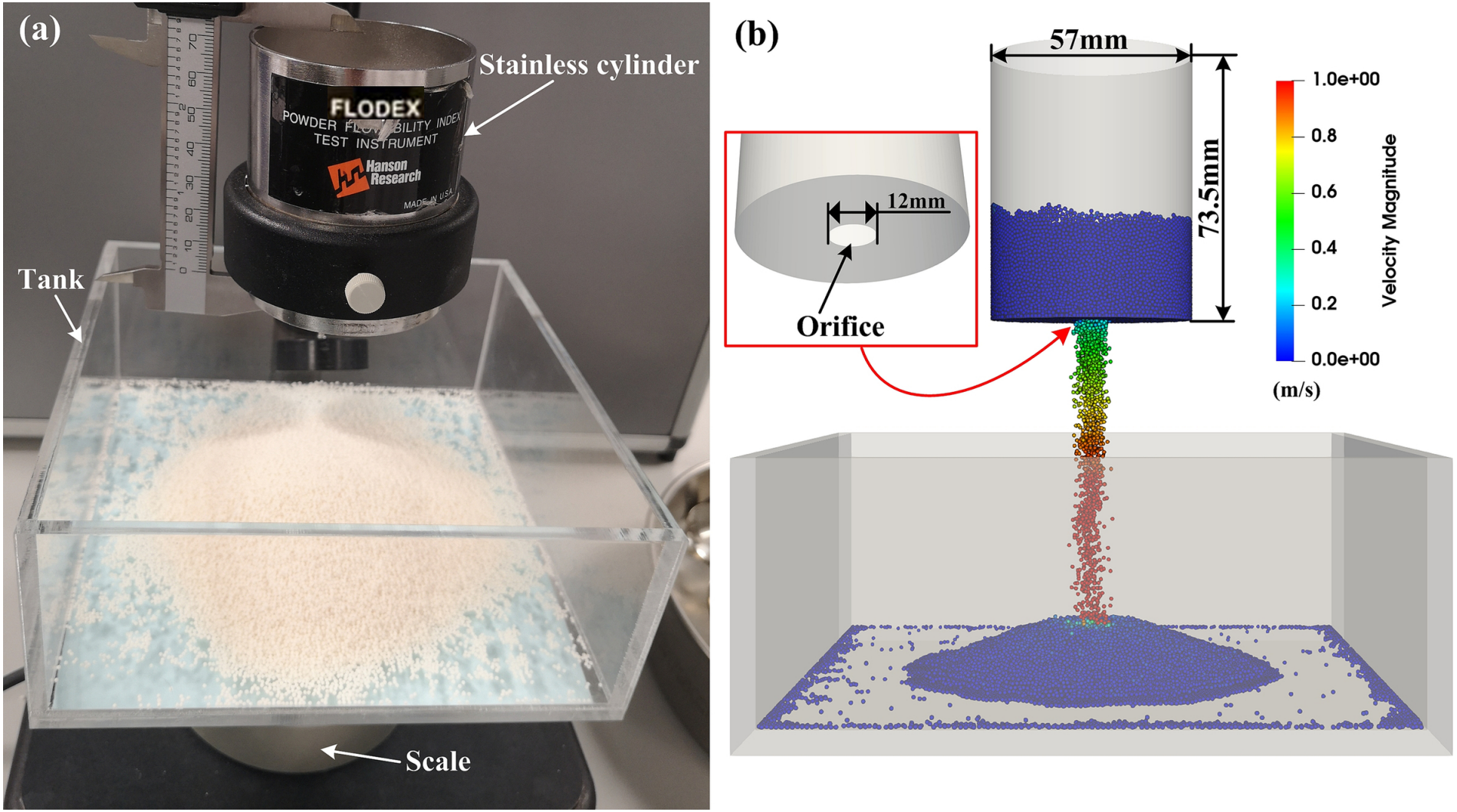
(a)
Stainless cylinder
FLODEX
POWDER FLOWABILITY INDEX
TEST INSTRUMENT
Hanson Research
MADE IN USA
Tank
Scale
(b)
57mm
73.5mm
12mm
Orifice
1.0e+00
0.8
0.6
0.4
0.2
0.0e+00
Velocity Magnitude
(m/s)

Figure 4

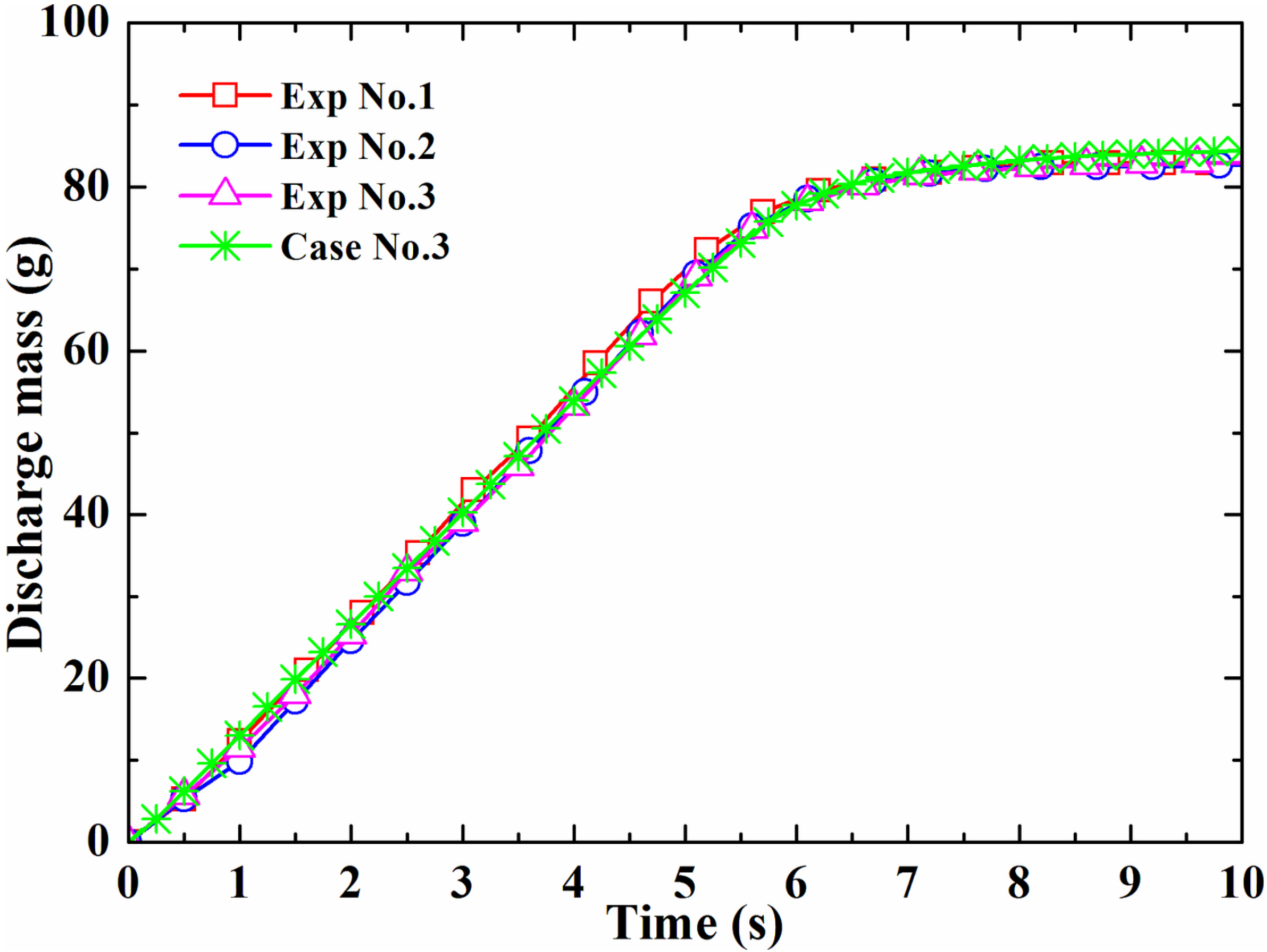
Exp No.1
Exp No.2
Exp No.3
Case No.3
Discharge mass (g)
Time (s)
0
20
40
60
80
100
0
1
2
3
4
5
6
7
8
9
10

Figure 5

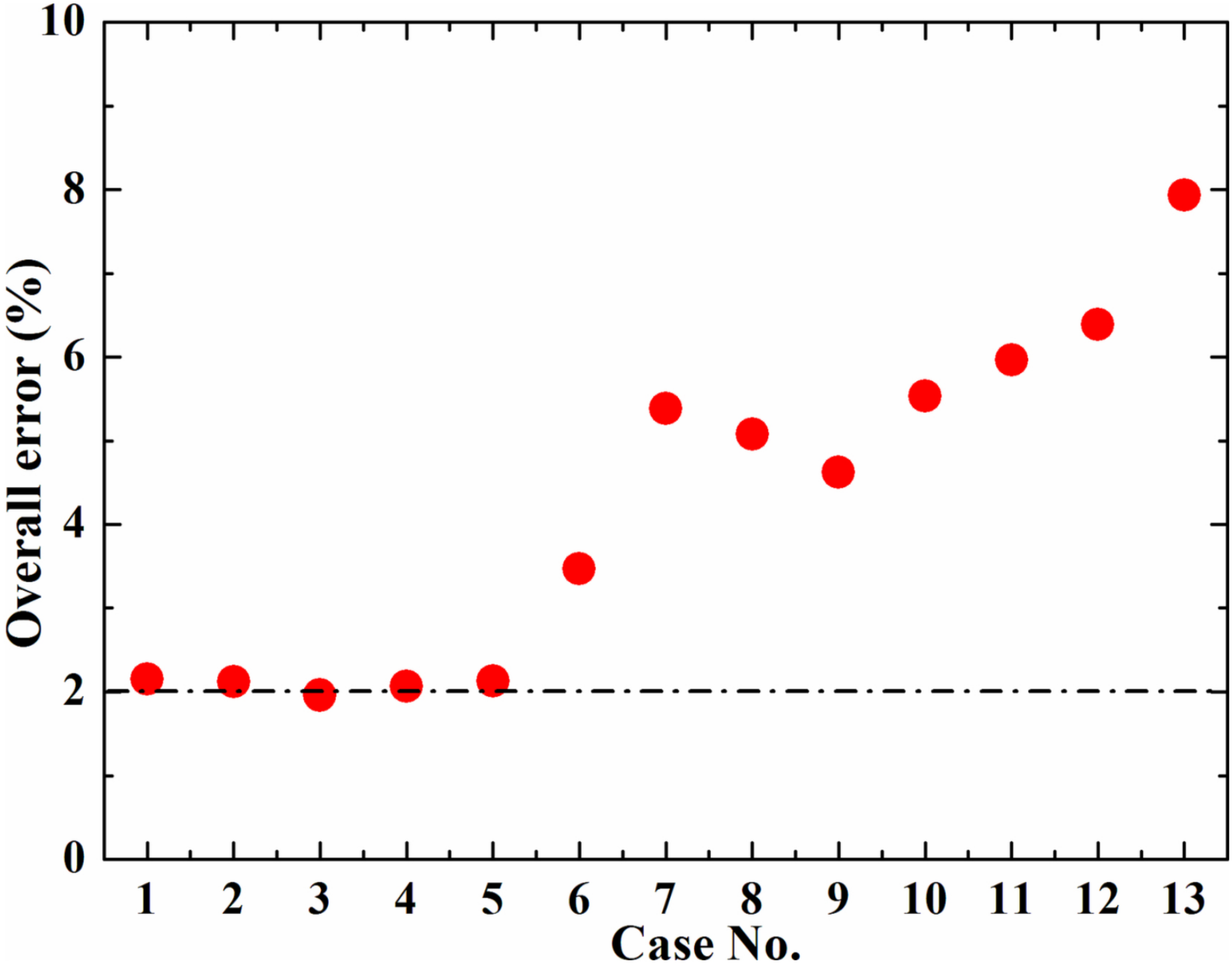

Figure 6

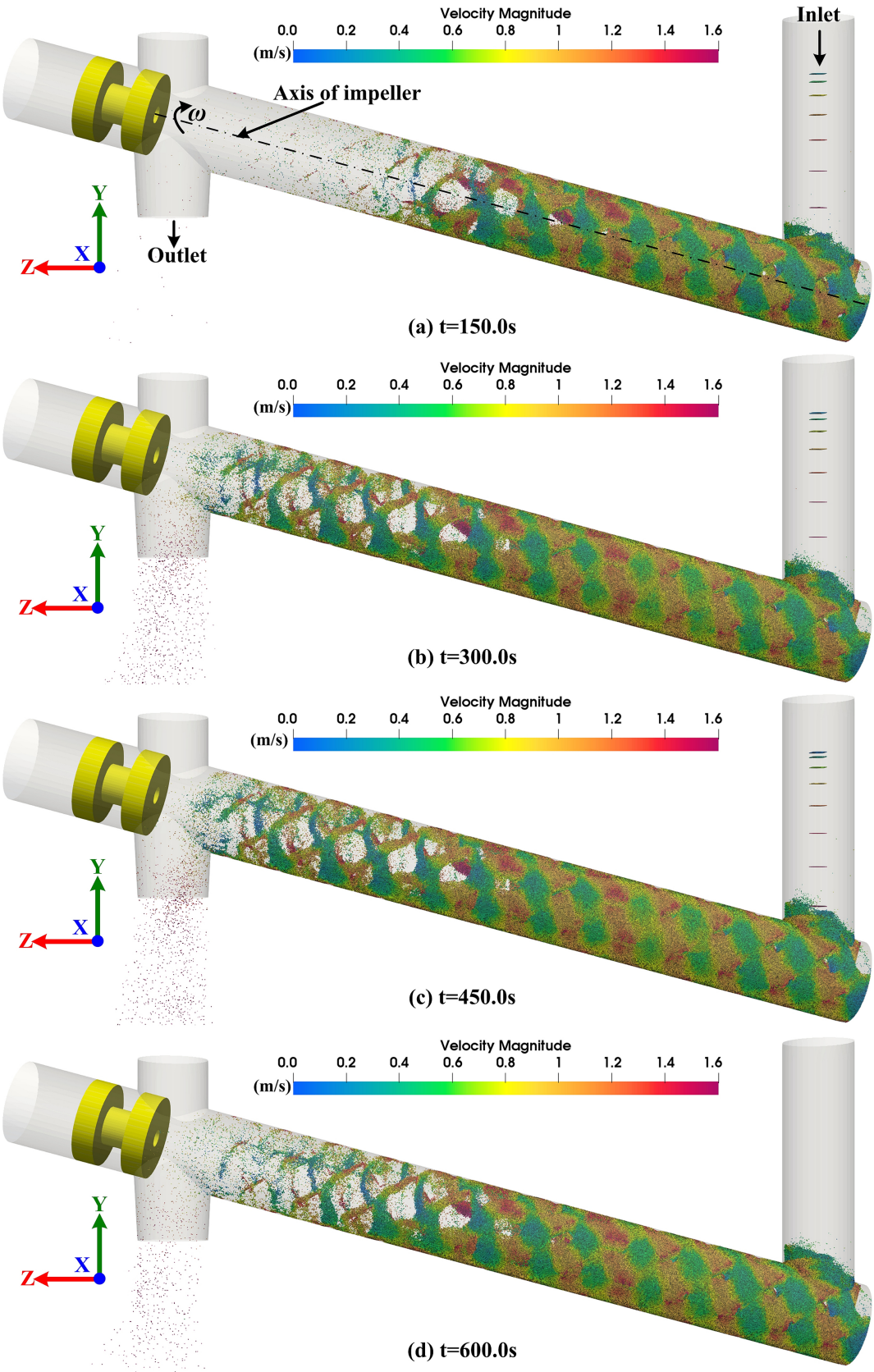
Velocity Magnitude
0.0 0.2 0.4 0.6 0.8 1 1.2 1.4 1.6
(m/s)
Inlet
Axis of impeller
ω
Outlet
Y
X
Z
(a) t=150.0s
(b) t=300.0s
(c) t=450.0s
(d) t=600.0s

Figure 7

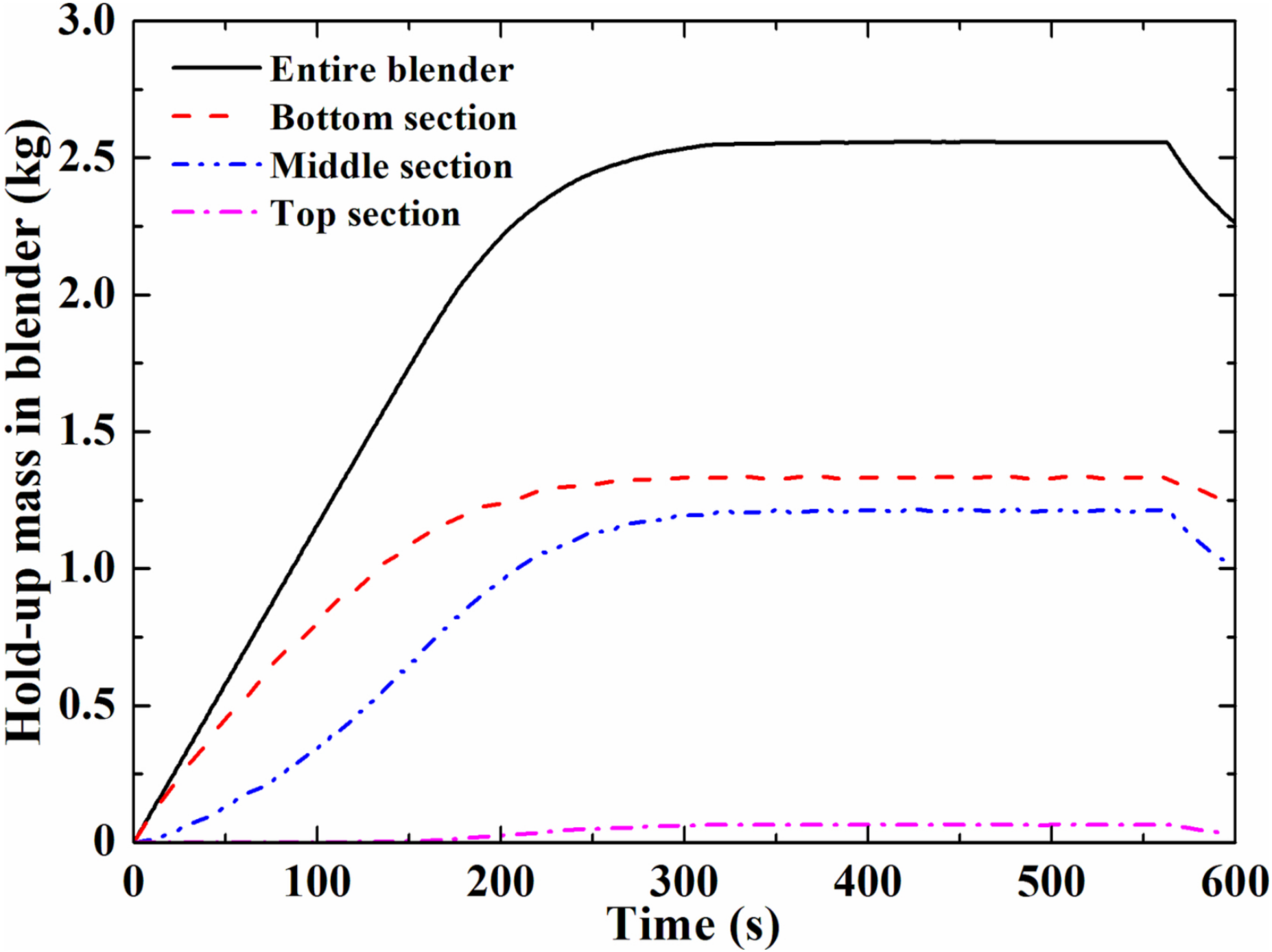
Entire blender
Bottom section
Middle section
Top section
Hold-up mass in blender (kg)
Time (s)
0
0.5
1.0
1.5
2.0
2.5
3.0
0
100
200
300
400
500
600

Figure 8

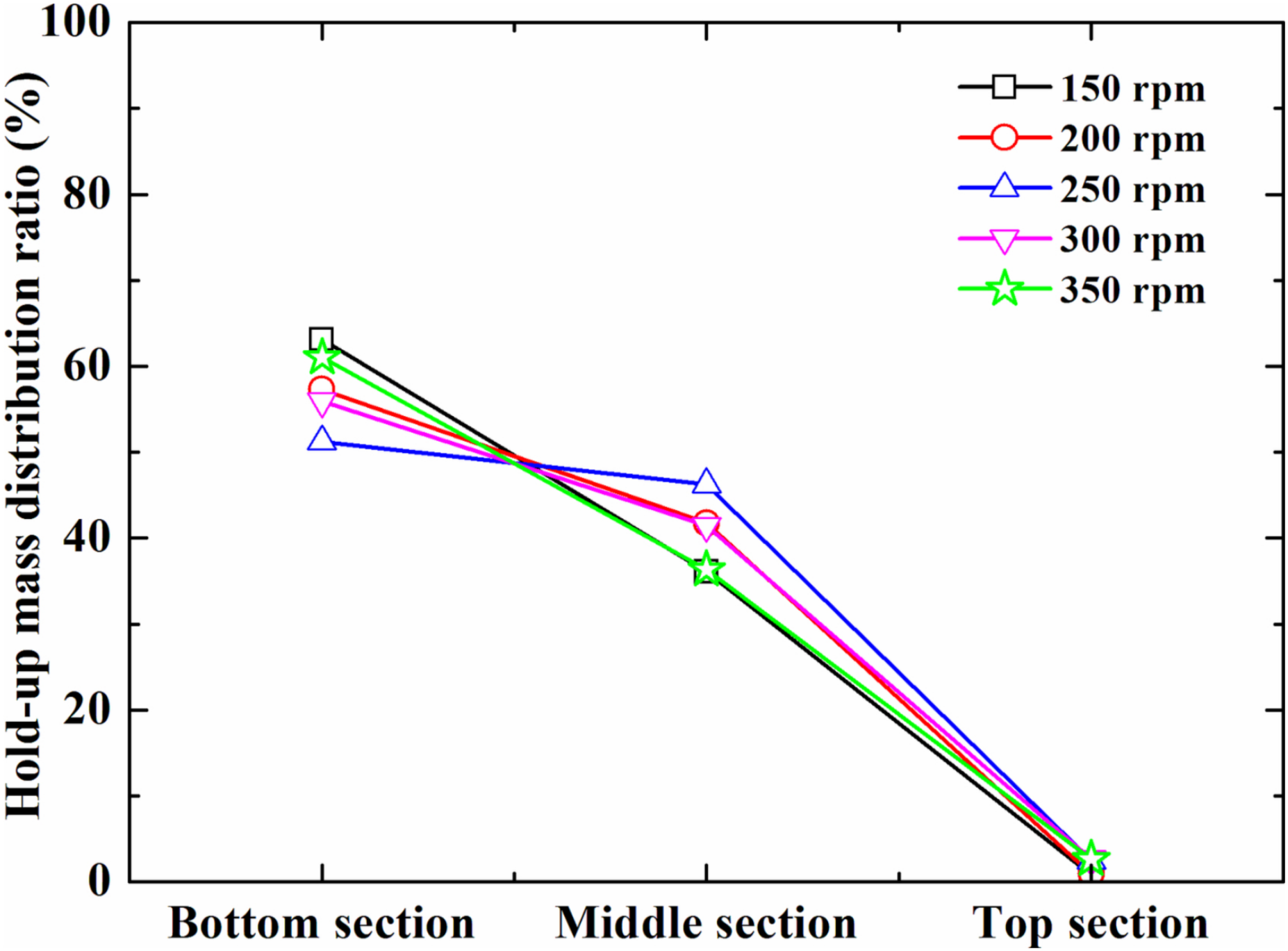
100
80
60
40
20
0
Hold-up mass distribution ratio (%)
150 rpm
200 rpm
250 rpm
300 rpm
350 rpm
Bottom section
Middle section
Top section

Figure 9

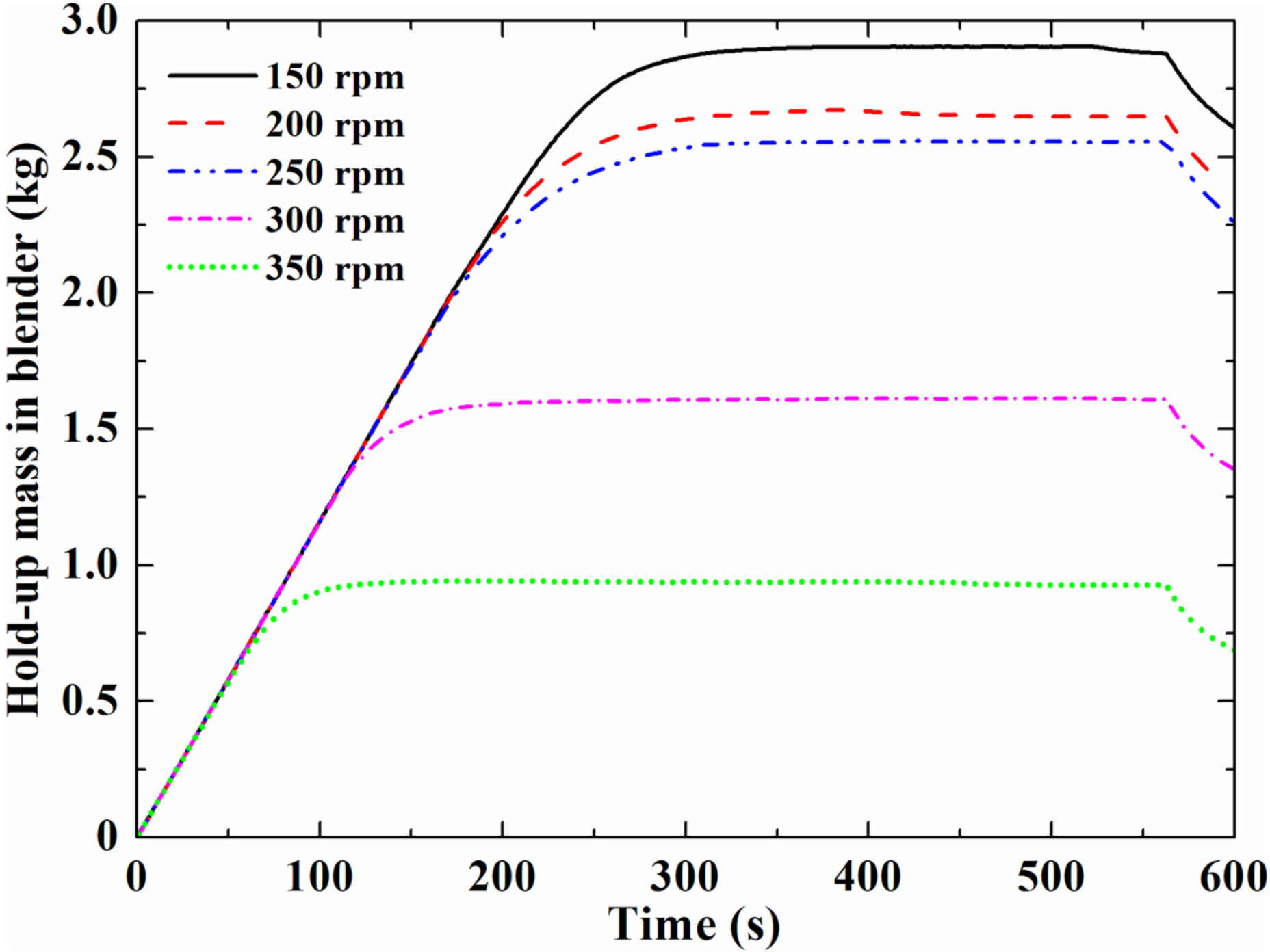
3.0
2.5
2.0
1.5
1.0
0.5
0
Hold-up mass in blender (kg)
150 rpm
200 rpm
250 rpm
300 rpm
350 rpm
0
100
200
300
400
500
600
Time (s)

Figure 10

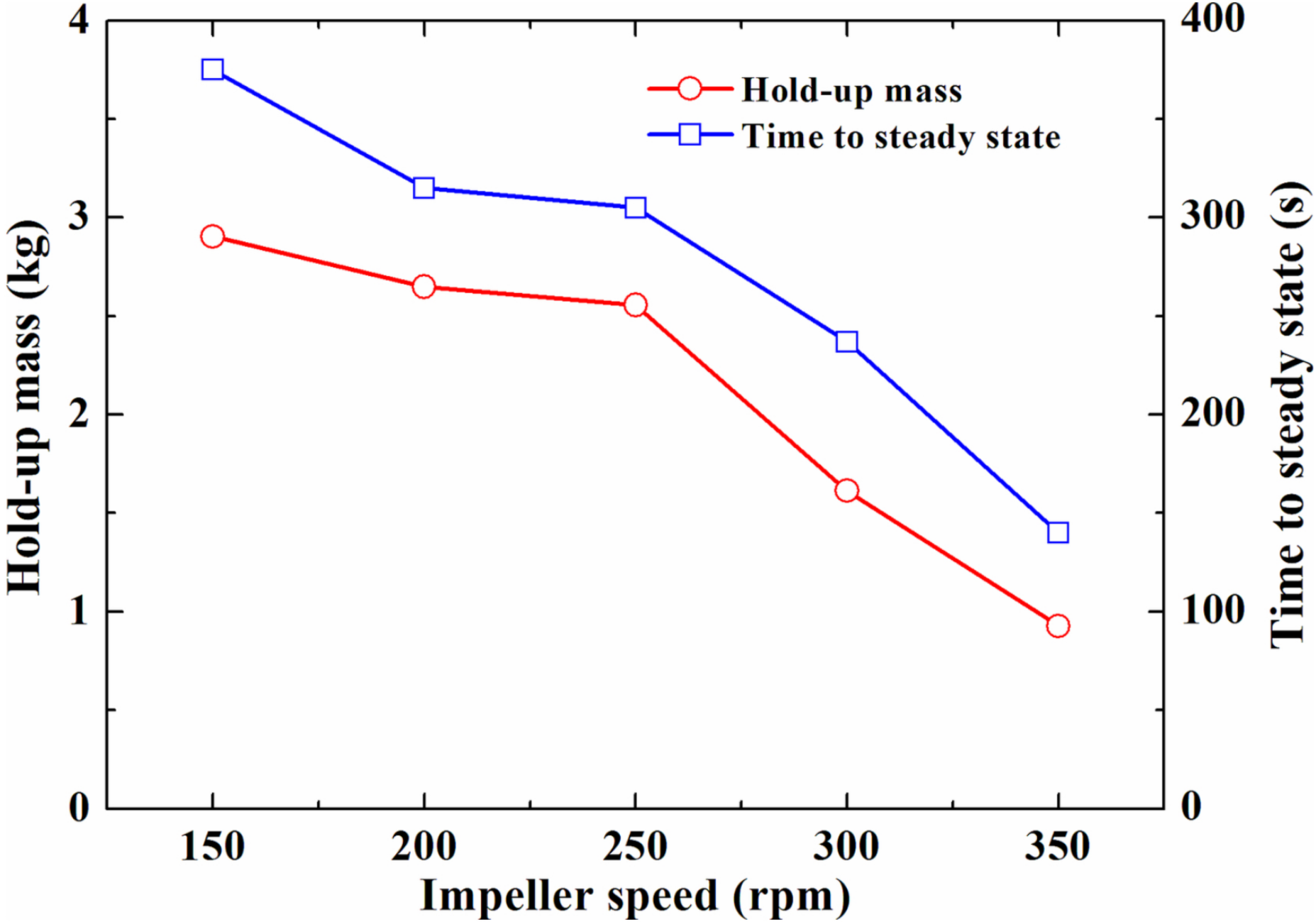
Hold-up mass
Time to steady state
Hold-up mass (kg)
Time to steady state (s)
Impeller speed (rpm)
0
1
2
3
4
0
100
200
300
400
150
200
250
300
350

Figure 11

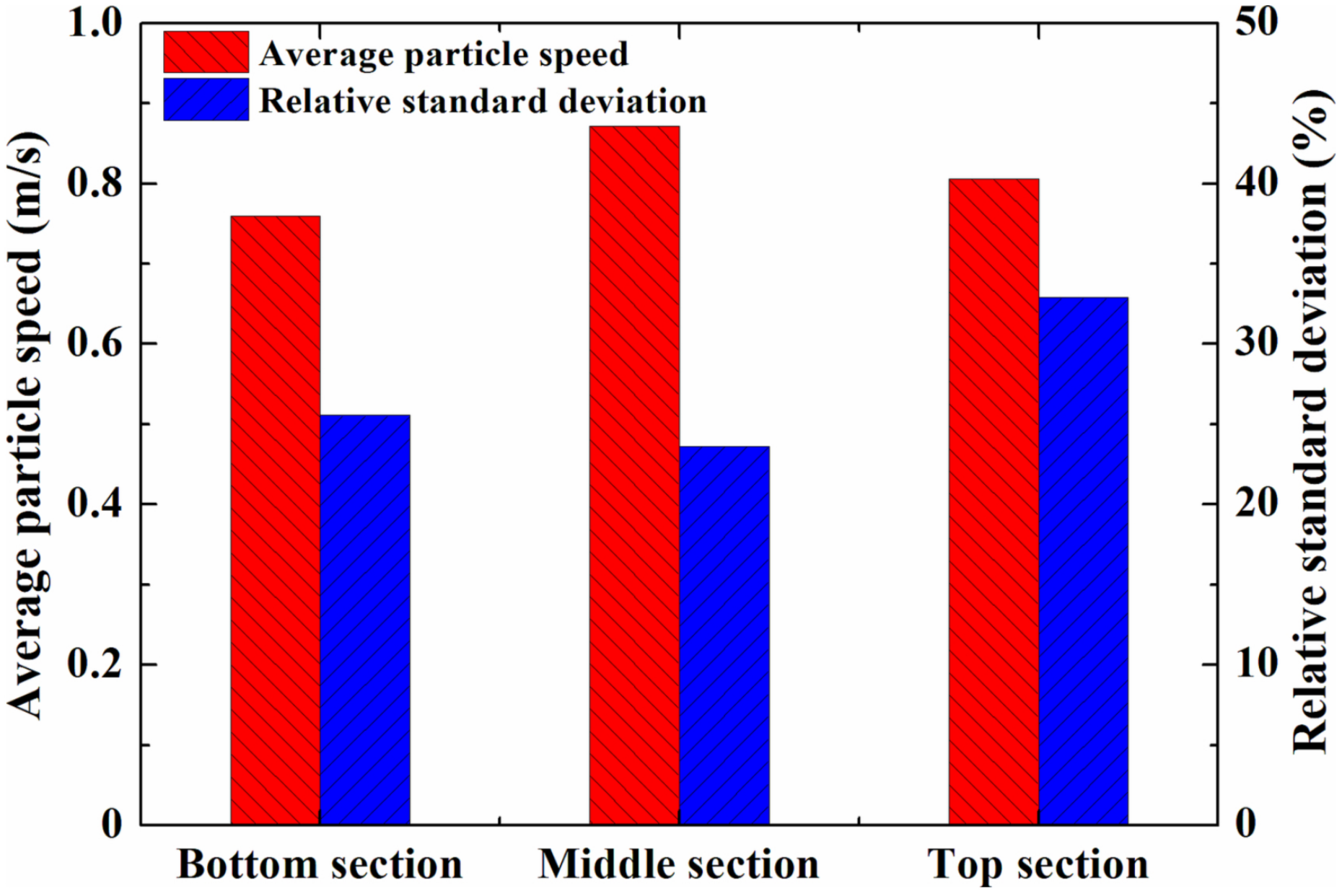
Average particle speed
Relative standard deviation
Average particle speed (m/s)
Relative standard deviation (%)
1.0
0.8
0.6
0.4
0.2
0
50
40
30
20
10
0
Bottom section
Middle section
Top section

Figure 12

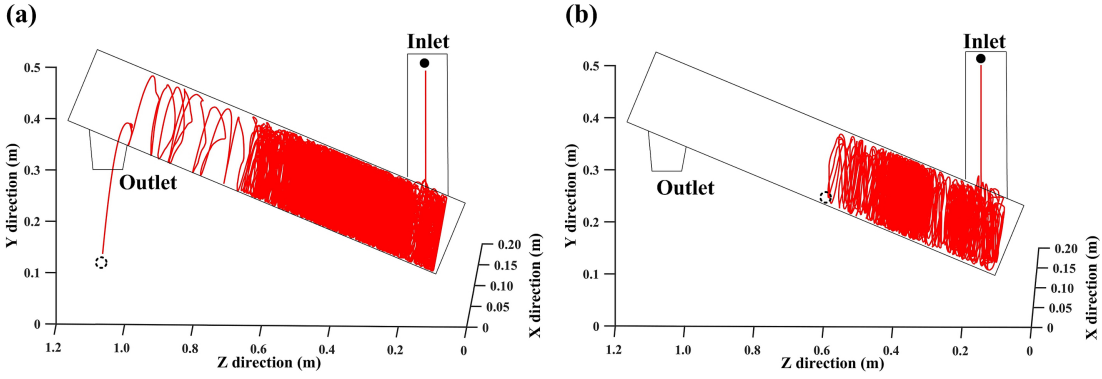
(a)
Inlet
Outlet
Y direction (m)
0.5
0.4
0.3
0.2
0.1
0
1.2
1.0
0.8
0.6
0.4
0.2
0
Z direction (m)
0.20
0.15
0.10
0.05
0
X direction (m)
(b)
Inlet
Outlet
Y direction (m)
0.5
0.4
0.3
0.2
0.1
0
1.2
1.0
0.8
0.6
0.4
0.2
0
Z direction (m)
0.20
0.15
0.10
0.05
0
X direction (m)

Figure 13

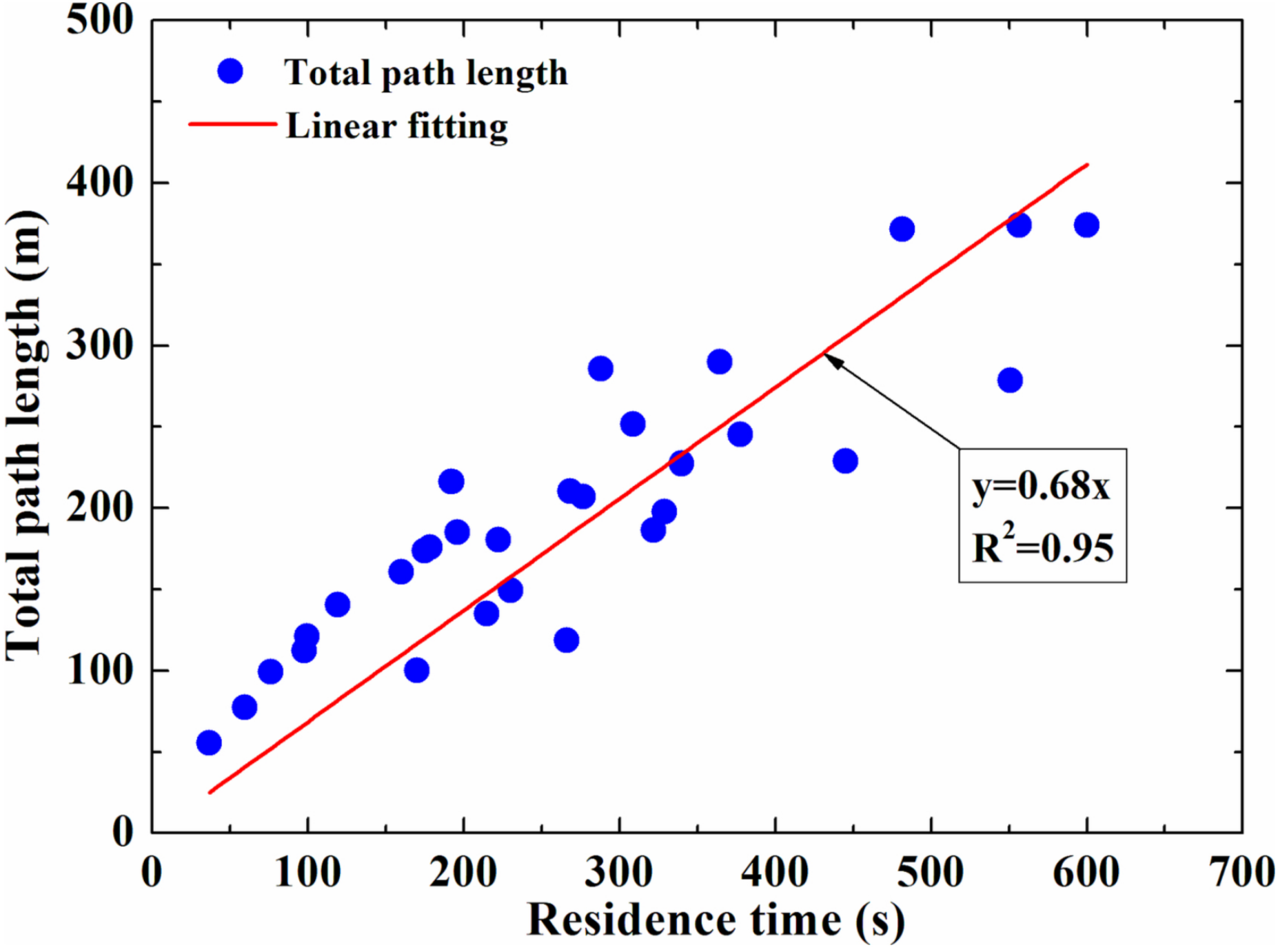
Total path length
Linear fitting
y=0.68x
R2=0.95
Total path length (m)
Residence time (s)
0
100
200
300
400
500
600
700

Figure 14

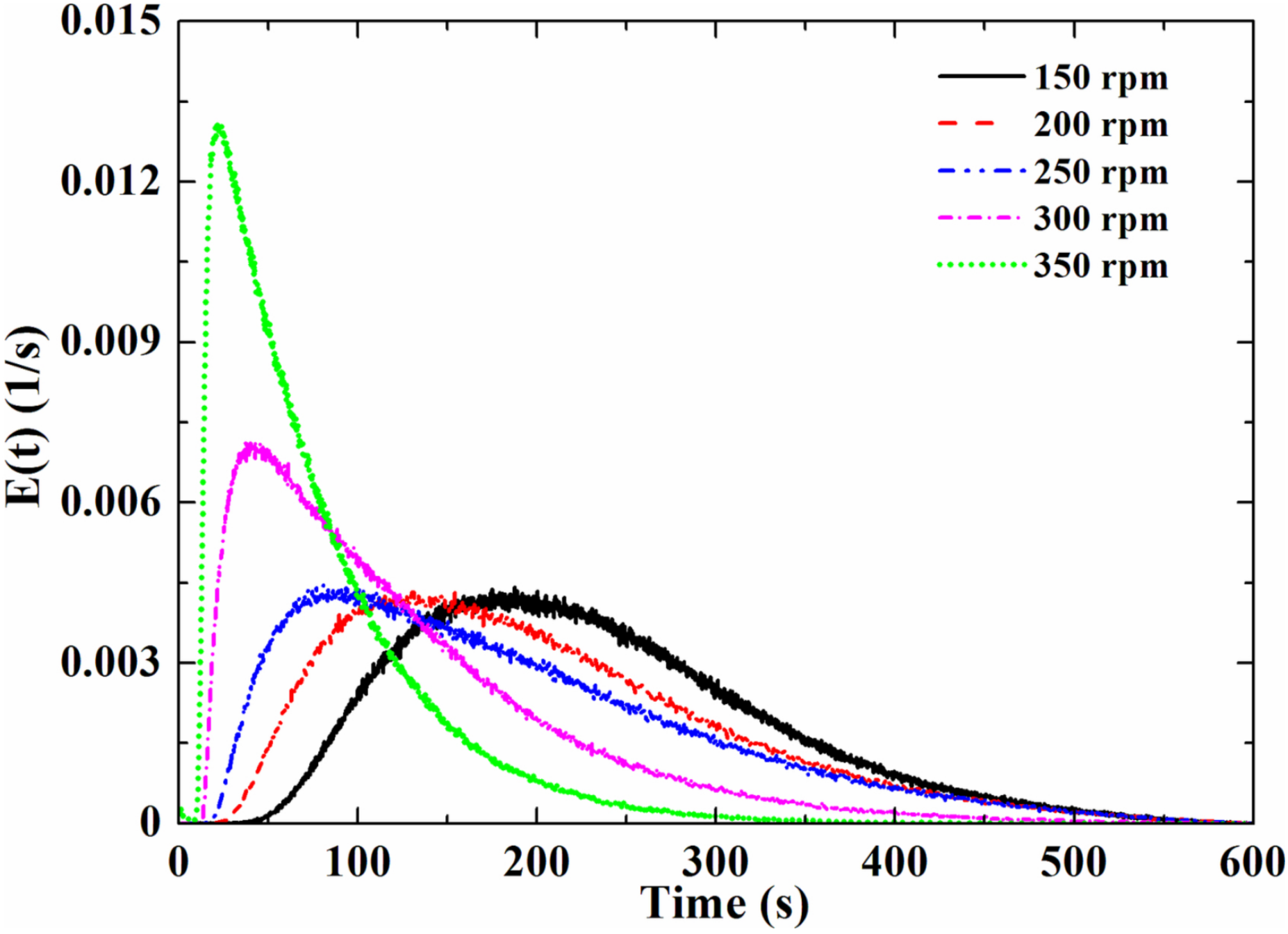
0.015
0.012
0.009
0.006
0.003
0
E(t) (1/s)
0
100
200
300
400
500
600
Time (s)
150 rpm
200 rpm
250 rpm
300 rpm
350 rpm

Figure 15

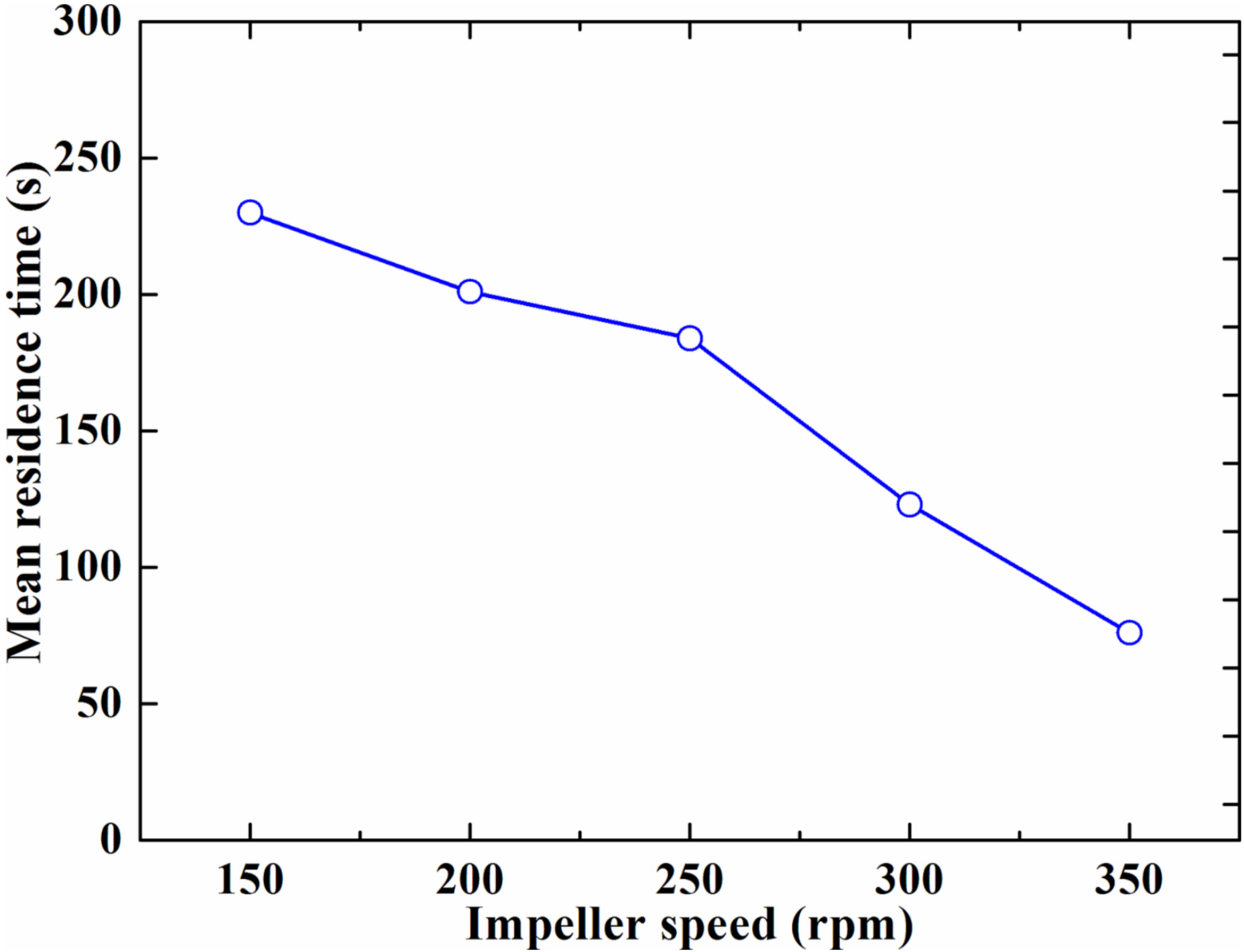
Mean residence time (s)
300
250
200
150
100
50
0
150
200
250
300
350
Impeller speed (rpm)

Figure 16

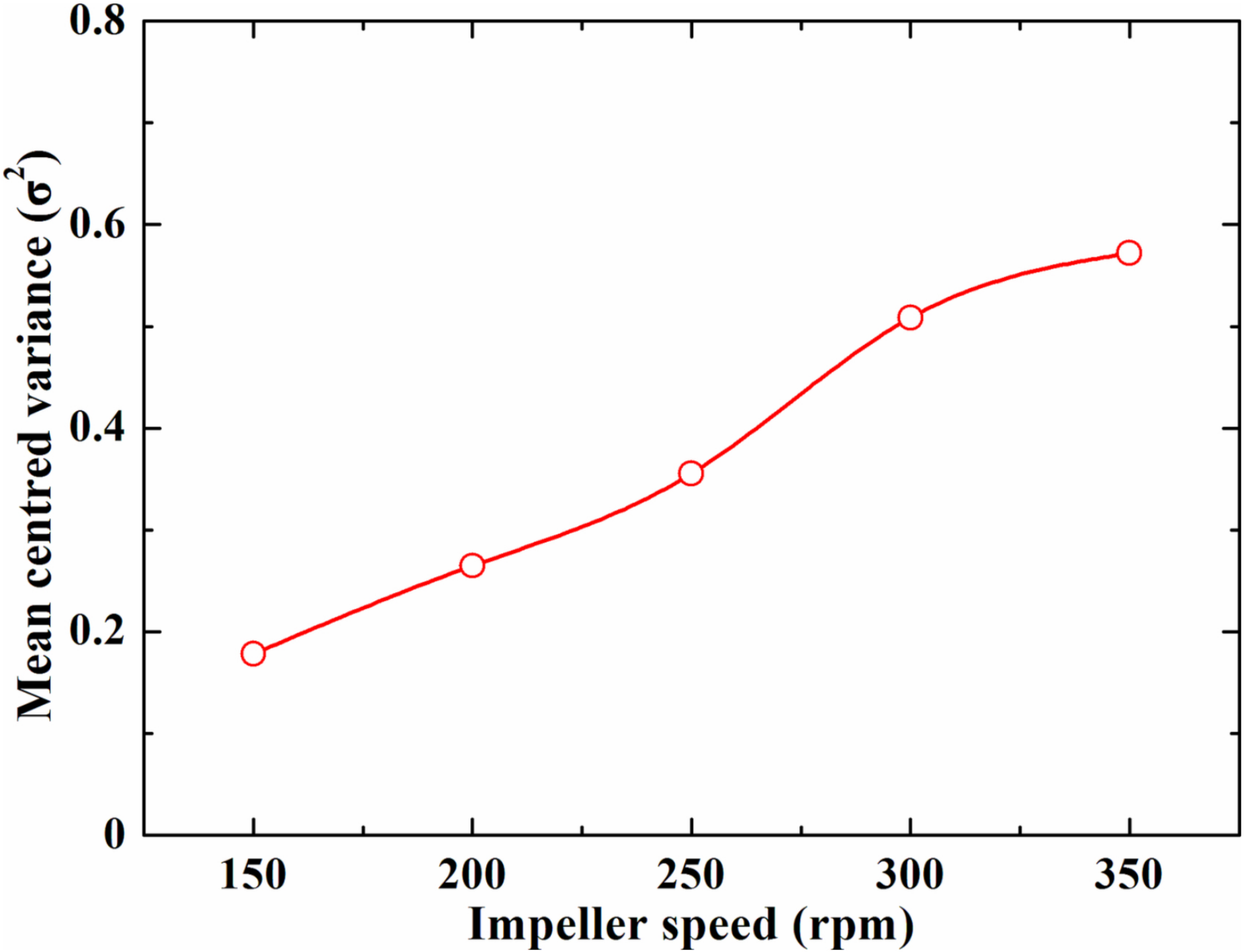
0.8
0.6
0.4
0.2
0
Mean centred variance (σ^2)
150
200
250
300
350
Impeller speed (rpm)

Figure 17

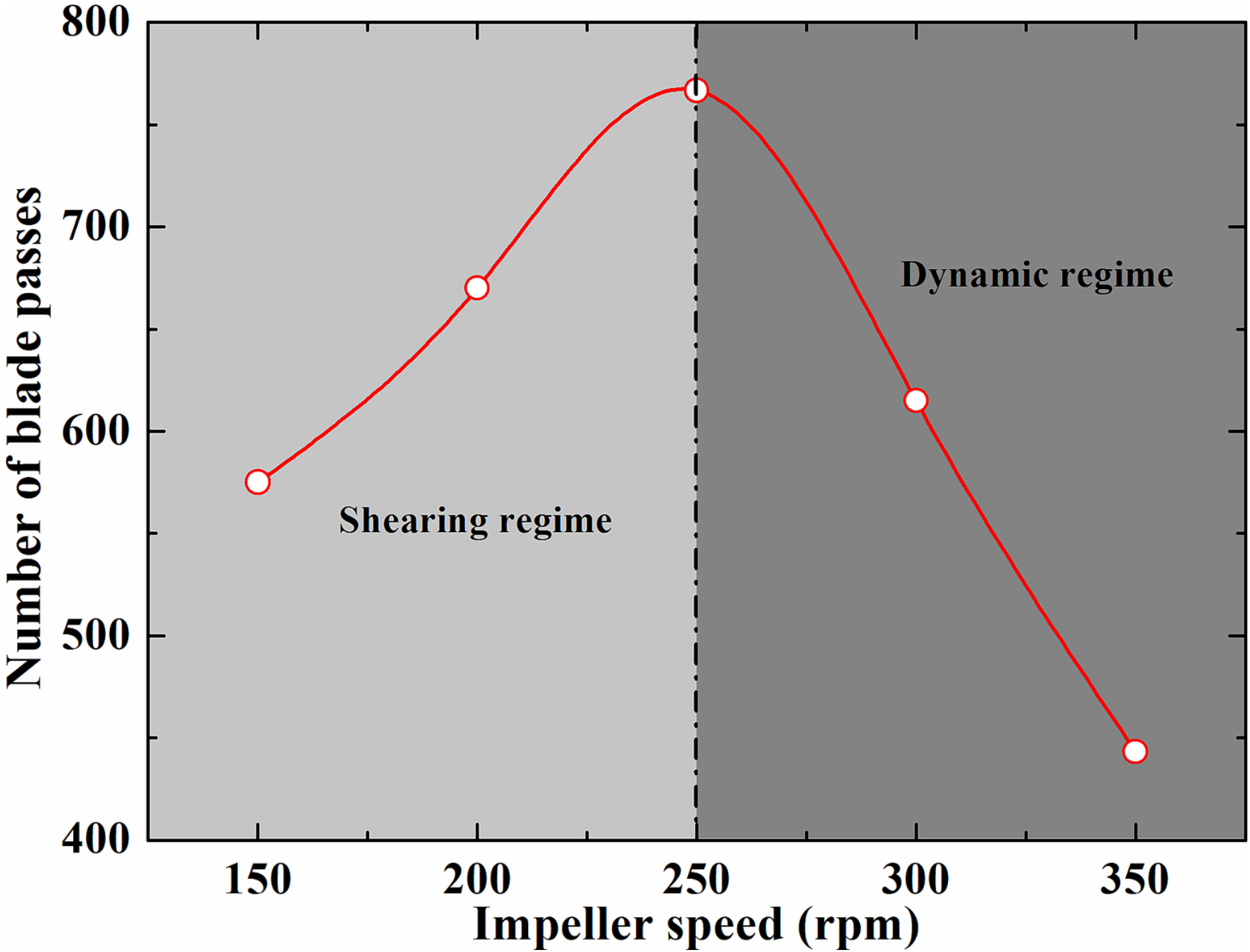
800
700
600
500
400
Number of blade passes
Shearing regime
Dynamic regime
150
200
250
300
350
Impeller speed (rpm)

Figure 18